Metals & corrosion

Phase-field analysis of anisotropic interfacial energy influence on microstructure evolution in directional and rotating directional solidification of ternary eutectics

Kaveh Dargahi Noubary[1,2,*] and Britta Nestler[1,2]

[1] *Institute of Digital Materials Science (IDM), Karlsruhe University of Applied Sciences (HKA), Moltkestraße 30, 76133 Karlsruhe, Baden-Württemberg, Germany*

[2] *Institute for Applied Materials - Microstructure Modelling and Simulation (IAM-MMS), Karlsruhe Institute of Technology, Straße am Forum 7, 76131 Karlsruhe, Baden-Württemberg, Germany*

ABSTRACT

The formation of cuboid fibers in Ni-Al-Mo and $[\alpha\beta]_a[\alpha\delta]_b$ superstructures in Bi-In-Sn ternary eutectics, driven by anisotropic interfacial energies, is investigated. To explain the formed superstructures (α, β and δ solid phase arrangement mechanism), a morphology map is developed based on Directional Solidification (DS) simulation results. It is assumed that phase omission potentially occurs in locked grains, where interface anisotropy influences microstructure evolution in the following manner: Anisotropic $\alpha\beta$ interfaces can drive the elimination of either the α or β layers in $\alpha\beta$ bilayers, while $\alpha\delta$ interface anisotropy can lead to the removal of either the α or δ layers in $\alpha\delta$ bilayers. This mechanism accounts for the formation of $\alpha\beta\alpha\delta$ motifs in quasi-isotropic grains and the emergence of $\alpha\beta\delta$ or $[\alpha\beta]_a[\alpha\delta]_b$ units in locked grains. It is additionally noted that $\alpha\beta$ anisotropy in locked grains exerts a stronger influence on microstructural development than $\alpha\delta$ anisotropy. Subsequent rotating DS (RDS) simulations provide additional supporting evidence for the assumed formation mechanisms. The radius profile of solidified floating grains exhibits a straight spiral pattern, whereas in locked grains, it follows a tilted spiral, with the tilt angle varying proportionally to anisotropy strength. Notably, the activation of anisotropy in any interface affects neighboring interfaces, even when they are modeled isotropically.

GRAPHICAL ABSTRACT
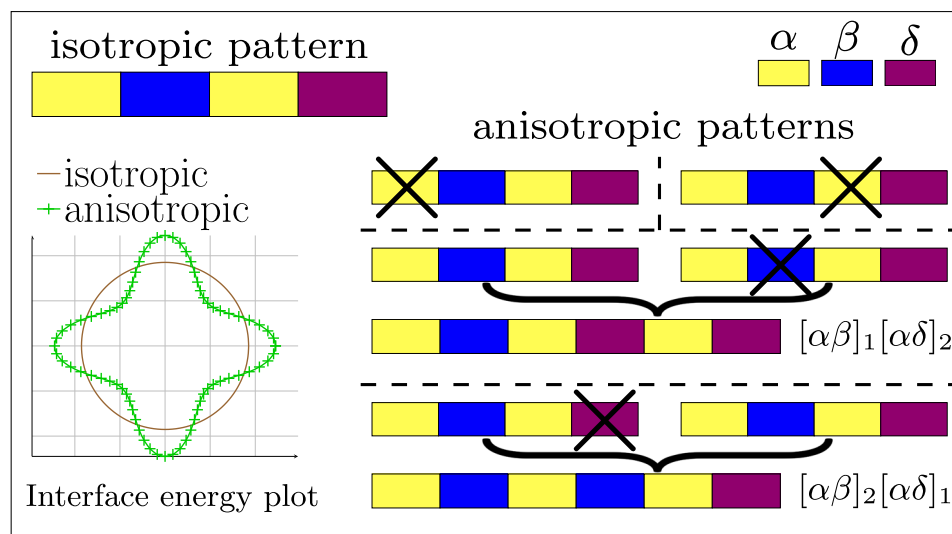
Introduction

The critical effects of anisotropic interfaces on pattern formation in Directional Solidification (DS) processes of various material systems have been widely studied [1–4]. DS experiments on the Ni-Al-Mo ternary eutectic by Zhang et al. [5] established fibrous microstructures, where Mo-rich fibers are embedded within NiAl-rich matrices. Anisotropic interfaces have been identified as a key factor in the formation of cuboid fibers instead of the commonly formed cylindrical rods. Among anisotropy-related studies, the Bi-In-Sn ternary eutectic has attracted interest due to its relatively low melting point ($\simeq 332$ K), which facilitates high-accuracy micrograph acquisition during experimental investigations [6–8]. The most common repeat unit in its solidified patterns is $\alpha\beta\alpha\delta$, where α represents the $BiIn_2$ crystalline phase, β the β-In crystalline phase, and δ the γ-Sn phase. Later studies [9, 10] revealed that interface anisotropy occurs in only some solidified grains, leading to the formation of $\alpha\beta\delta$ and $[\alpha\beta]_a[\alpha\delta]_b$ superstructures ($a, b \in \mathbb{N}, a \neq 1 \vee b \neq 1$). The system tends to revert to the stable $\alpha\beta\alpha\delta$ pattern through mechanisms such as *phase exchange* (see Fig. 14 of [10]) and *continuous elimination of all phases* (Fig. 7 of [10]). In addition, changes in solidification velocity introduce further instabilities, such as *lamellae branching* and *lamellae elimination*. Lamellae branching occurs when velocity surpasses a threshold, while elimination happens when it drops below the system's minimum velocity limit. Other reported instabilities in anisotropic grains include tilted phase growth relative to the applied temperature gradient [11–13] and oscillatory solid phase boundary behavior [14]. Studies by Mohagheghi et al. [15] classify isotropic grains as *floating grains* and strongly anisotropic grains in which the phase arrangement is affected, as *locked grains*. *Quasi-isotropic* grains refer to grains that exhibit interfacial anisotropy, but its influence is insufficient to alter the phase arrangement. This underscores why understanding the impact of anisotropic interface properties on microstructure evolution remains a key research focus.

To explore these effects, the Rotating Directional Solidification (RDS) method [16, 17] has been introduced alongside DS. In RDS, sample holder rotation induces circular trajectories in the solidified phases. These trajectories in locked grains appear tilted relative to the imposed temperature gradient. The influence of $\alpha\beta$ interface anisotropy on pattern formation is found to be more significant than that of $\alpha\delta$ interface anisotropy [15]. While experiments reveal many

details about solidification mechanisms, they can face challenges in isolating the effects of individual material parameters. Conversely, simulations of phase transformations and eutectic pattern formation can provide a controlled environment for systematically investigating these influences [18, 19]. In our previous studies, we simulated eutectic reactions in NiAl-10Mo [20] and Bi-In-Sn [21] ternary systems using PACE3D framework [22, 23]. In this notation, NiAl-10Mo refers to the eutectic transition within the Ni-Al-Mo ternary system, characterized by an isopleth section. Gibbs energy G formulations were approximated using Thermo-Calc software [24], with data extracted from CALPHAD databases [25, 26]. Based on the introduced energy approximation technique in [20], the energy expressions were formulated as second-order polynomials taking into account the essential thermodynamic criteria: $G(c_1, c_2, T) = A_1(T) \cdot c_1^2 + A_2(T) \cdot c_2^2 + A_3(T) \cdot c_1 \cdot c_2 + A_4(T) \cdot c_1 + A_5(T) \cdot c_2 + A_6(T)$. In this formulation, $A_1(T), \ldots, A_6(T)$ are the linear temperature-dependent functions based on the system properties and c_1, c_2 are independent concentration values in the investigated ternary system ($c_3 = 1 - c_1 - c_2$). For NiAl-10Mo, two-dimensional (2D) simulations of DS showed stable growth of Mo-rich fibers within NiAl-rich matrices [20], assuming isotropic interfacial energies. Three-dimensional (3D) simulations are essential to investigate the role of interfacial anisotropy in this system. While such simulations are not entirely unprecedented, related efforts in the literature remain limited. Dejmek et al. [27] performed phase-field simulations to analyze the stability limits of hexagonal cells and eutectic lamellae, demonstrating that as in 2D models, crystalline anisotropy significantly influences morphological stability. In highly anisotropic cases, they observed lamellar breakup. In the work of Ma et al. [28], phase-field modeling of silicon solidification revealed facet formation driven by the interplay between the dynamic anisotropy and the interface energy anisotropy. Gurevich et al. [29] investigated steady-state growth shapes in an idealized binary alloy, showing a transition from finger-like to needle-like fibers with increasing growth velocity. The present work on the NiAl-10Mo eutectic system explores a distinct morphological transition in 3D.

In [21], the eutectic reaction in Bi-In-Sn was simulated using both DS and RDS techniques. The DS simulations considered a domain width of one lamellar spacing with initial solid α, β, and δ phases arranged in $\alpha\beta\alpha\delta$, in contact with the liquid phase, all modeled isotropically. Consequently, two RDS simulations were conducted one assuming isotropic interfaces and another incorporating anisotropy in a specific configuration. The experimentally observed circular trajectories were resulted including inclined solid-phase growth in locked grains. Results for both material systems were validated through Jackson-Hunt analysis [30] and comparison with the experimental data.

This work extends the previous simulations through a systematic study, varying system parameters stepwise. Anisotropy of the solid-solid interfacial energies is activated and its strength is varied in different simulation series. The DS and RDS results are found to be complementary in revealing the persistent mechanisms in the microstructure evolutions. The evolved patterns are analyzed, and a morphology map explaining their formation is introduced.

Phase-field formulation

Eq. (1) governs the temporal evolution of phases $\partial \phi_{\hat{\alpha}}(\vec{x}, t)/\partial t$ which is derived from grand-potential functionals according to [31–34], widely used in material system simulations [35–38].

$$\tau \varepsilon \frac{\partial \phi_{\hat{\alpha}}}{\partial t} = \underbrace{-\varepsilon \left(\frac{\partial a(\boldsymbol{\phi}, \nabla \boldsymbol{\phi})}{\partial \phi_{\hat{\alpha}}} - \nabla \cdot \frac{\partial a(\boldsymbol{\phi}, \nabla \boldsymbol{\phi})}{\partial \nabla \phi_{\hat{\alpha}}} \right) - \frac{1}{\varepsilon} \frac{\partial w(\boldsymbol{\phi})}{\partial \phi_{\hat{\alpha}}}}_{:=rhs_{1,\hat{\alpha}}}$$
$$\underbrace{- \frac{\partial \psi(\boldsymbol{\phi}, \boldsymbol{\mu}, T)}{\partial \phi_{\hat{\alpha}}}}_{:=rhs_{2,\hat{\alpha}}} \underbrace{- \frac{1}{N} \sum_{\hat{\beta}=1}^{N} (rhs_{1,\hat{\beta}} + rhs_{2,\hat{\beta}})}_{\text{Lagrangeparameter}}$$

(1)

Here, $\phi_{\hat{\alpha}}$ represents an individual phase-field in the vector $\boldsymbol{\phi}$. The gradient energy density $a(\boldsymbol{\phi}, \nabla \boldsymbol{\phi})$ and potential energy density $w(\boldsymbol{\phi})$ include interfacial energies $\gamma_{\hat{\alpha}\hat{\beta}}$ and a higher-order term $\gamma_{\hat{\alpha}\hat{\beta}\hat{\delta}}$ to prevent third-phase formation at binary interfaces [35]. Greek letters α, β denote phases, while hatted versions $\hat{\alpha}, \hat{\beta}$ distinguish the phase names from sigma indices. τ is the material-specific kinetic parameter, ε is an interface-width-related factor, and ψ represents the driving force as a function of phase-fields, chemical

potentials $\boldsymbol{\mu}$, and temperature T. The Lagrange parameter serves to uphold the constraint $\sum_{\hat{\alpha}=1}^{N} \phi_{\hat{\alpha}} = 1$. The chemical potential vector evolves per Fick's law and mass conservation as formulated in Eq. (2) [33].

$$
\begin{aligned}
\frac{\partial \boldsymbol{\mu}}{\partial t} = &\left[\sum_{\hat{\alpha}=1}^{N} h_{\hat{\alpha}}(\boldsymbol{\phi}) \left(\frac{\partial \boldsymbol{c}_{\hat{\alpha}}(\boldsymbol{\mu}, T)}{\partial \boldsymbol{\mu}} \right) \right]^{-1} \\
&\left(\nabla \cdot \left(\boldsymbol{M}(\boldsymbol{\phi}, \boldsymbol{\mu}, T) \nabla \boldsymbol{\mu} - \boldsymbol{J}_{at}(\boldsymbol{\phi}, \boldsymbol{\mu}, T) \right) \right. \\
&- \sum_{\hat{\alpha}=1}^{N} \boldsymbol{c}_{\hat{\alpha}}(\boldsymbol{\mu}, T) \frac{\partial h_{\hat{\alpha}}(\boldsymbol{\phi})}{\partial t} \\
&\left. - \sum_{\hat{\alpha}=1}^{N} h_{\hat{\alpha}}(\boldsymbol{\phi}) \left(\frac{\partial \boldsymbol{c}_{\hat{\alpha}}(\boldsymbol{\mu}, T)}{\partial T} \right) \frac{\partial T}{\partial t} \right)
\end{aligned}
\tag{2}
$$

In Eq. (2), $\boldsymbol{M}, \boldsymbol{c}$ and $h(\boldsymbol{\phi})$ are mobility matrix, concentration vector and the interpolate function between the co-existing phases as defined in [39]. The grand chemical potential (GP) is defined as $GP = G - \mu \cdot c$ [31]. **Interfacial anisotropy** is incorporated in the formulation of the gradient energy density contribution $a(\boldsymbol{\phi}, \nabla \boldsymbol{\phi})$ which is discussed in detail in **Appendix A**. $\boldsymbol{J}_{at}$ is the anti-trapping current to suppress the artificially enlarged interface widths in model, compared to experimental data.

For third-phase nucleation (e.g., δ) at solid–liquid interfaces (e.g., α-l), the following mechanism applies:

$$
\xi_{\delta} = \begin{cases} n_{\text{dist}} \cdot A & \forall \phi_{\alpha} \phi_l > 0, \quad dt \bmod i = 0 \\ 0 & \text{else.} \end{cases}
\tag{3}
$$

The noise term ξ_{δ} is incorporated into Eq. (1) as described in [40, 41]. Nucleation is triggered when noise-induced concentration deviations exceed a threshold c_{limit}, evaluated after i time steps dt. Here, A controls noise amplitude, and n_{dist} distributes noise uniformly. Applications of this mechanism are found in [42, 43]. The temperature in the DS simulations T^{DS} is modelled as a constant but moving temperature field, given by Eq. (4). The effects of hot and cold blocks as well as the linear motion of the sample holder in the experimental machine [10] are described by the employed parameters in this formulation. T_0 stands for a base temperature, G^{DS} is the temperature gradient, v the solidification velocity and x is the pulling direction, respectively. Temperature gradients perpendicular to x are assumed negligible.

$$
T^{\text{DS}}(x, t) = T_0 + G^{\text{DS}}(x - vt)
\tag{4}
$$

The temperature-evolution equation in RDS has to resemble the effects of rotating sample holder on the temperature variation in sample. T^{RDS} in Eq. (5) shows such a configuration in which T_m stands for the temperature in the rotating disk center and A_0 is a constant coefficient to control the maximum and minimum temperature values in the simulation domain.

$$
T^{\text{RDS}}(x, y, t) = T_m + A_0 \cdot \tan^{-1} \left[\frac{G^{\text{RDS}}}{A_0} \left(x \cdot \sin(\omega t) + y \cdot \cos(\omega t) \right) \right]
\tag{5}
$$

G^{RDS} is the temperature gradient and ω stands for the angular velocity of the rotating disk [21]. In DS, the steady-state heat equation ($\nabla^2 T^{\text{DS}} = 0$) holds due to the linear spatial dependence of temperature. Although in T^{RDS} such linear dependency is absent, the deviation of $\nabla^2 T^{\text{RDS}}$ from zero becomes negligible with the utilized process parameters in the current configuration as implied in [21].

Simulations and results

In Sect. 3.1, following the simulations conducted in [20], a representative NiAl-10Mo simulation is extended from two to three dimensions, and the previously isotropic interface is modeled anisotropically. The primary objective is to isolate the unique impact of the anisotropic solid/solid interface on the formed pattern, and compare it with the referenced experimental micrographs.

Next, the Bi-In-Sn system is investigated, where the implemented two-dimensional DS and RDS simulations from [21] are extended as follows:

(i) In Sect. 3.2, the DS simulations are performed on a domain size increased tenfold, with random distribution of initial α, β, and δ solid-phase seeds in contact with the liquid phase. The nucleation mechanism is additionally activated, further enhancing the free-arrangement capability in solidifying microstructure. A systematic study of the influence of anisotropy strength on the final evolved patterns is conducted. Based on the results, a morphology map is proposed to explain the observed patterns.

(ii)   In Sect. 3.3, complementary anisotropic RDS simulations are carried out, driven by the need identified in (i). Anisotropy strength is varied stepwise, and the resulting microstructures are analyzed. The proposed map proves useful in explaining the observed patterns, despite the noticed limitations in its explanatory power.

Three-dimensional DS simulation for NiAl-10Mo system

The samples in the DS experiments by Zhang et al. [5] are exposed to a temperature gradient of $G^{DS} = 33.4 \, Kmm^{-1}$ and solidification velocities in the range of $2 - 300 \, \mu ms^{-1}$. More well-aligned and regular eutectic structures are formed for velocities up to $35 \, \mu ms^{-1}$, resulting in hexagonal fiber arrangements with rectangular cross-sections. For higher velocities interfaces with cellular morphologies were identified instead of previously formed planar interfaces. In this section, the solidification velocity $30 \, \mu ms^{-1}$ is used for a three-dimensional simulation, as it is the highest velocity investigated in the previous study and demands relatively low computational power. Figure 1 shows the simulation results after 8.35×10^6 time steps using 54 CPUs. To achieve a 3D phase

arrangement in the rectangular-prism domain, a predefined phase configuration is set, including one cylindrical fiber at the center and four quarter-cylinders at each corner. With periodic boundary conditions along the sides of the simulation domain perpendicular to the growth direction, a hexagonal fiber arrangement is obtained by mirroring the domain across xy and xz planes. The average rod spacing, $\lambda_{ave}^{R} = 1.106 \, \mu m$, as reported in [5], is used here as well. The sections in Fig. 1 correspond to cross-sectional areas at different growth distances. Dashed rectangles highlight the initial fiber configuration (yellow Mo-rich fibers in a cyan NiAl-rich matrix) before mirroring. The material and process parameters for this simulation are summarized in Table 2 of Appendix B. Similar to the 2D models, initial oscillations at the matrix-fiber interface occur as the solid–liquid interface transitions from flat to curved. These oscillations appear at a growth distance of $x \simeq 0.65 \, \mu m$, with the fiber cross-sections in the intermediate transition state from squares to circles. As growth continues, the transition is completed, which remains consistent until the end of the simulation. This demonstrates that the current phase-field model, incorporating the cubic anisotropy, successfully captures the effect of orientation-dependent interfacial energies on the formation of cuboid fibers in the NiAl-10Mo ternary eutectic.
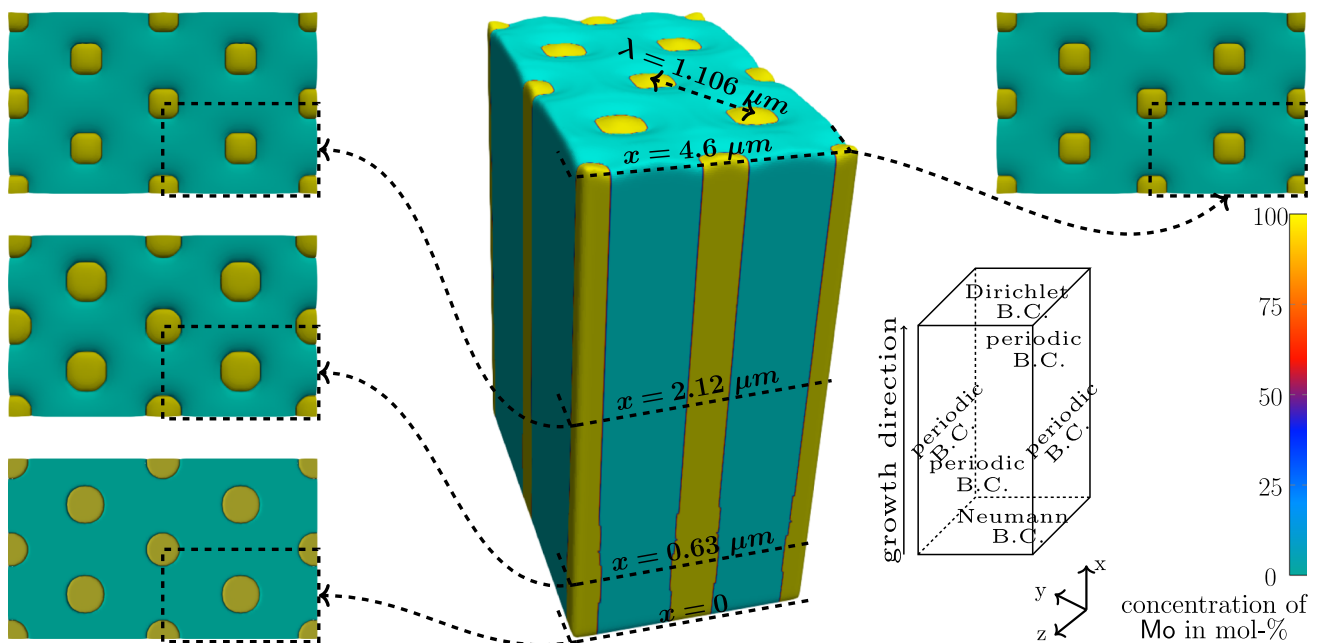

Figure 1 The eutectic solidification of the NiAl-10Mo ternary system resulted in a 3D microstructure. In magnified sections, the transformation of fibers from cylindrical to cuboid shapes is monitored, driven by anisotropic interface effects..

DS simulations of the Bi-In-Sn system

The process conditions for DS simulations of the Bi-In-Sn system in [21] are based on experiments by Witusiewicz et al. [7]. The experimental inputs include a solidification velocity of $v = 0.5 \ \mu ms^{-1}$, a temperature gradient of $G^{DS} = 8 \ Kmm^{-1}$, and an average lamellar spacing $\lambda^L_{ave} = 23.4 \ \mu m$. In Fig. 4 of [21], the simulation result for a domain width equal to one lamellar spacing is presented. In this work, the simulation domain width is increased tenfold equal to 234 μm, and the initial solid phases are subjected to the liquid phase using Voronoi tessellation [44, 45]. This leads to a random distribution of small solid-phase particles. These small particle sizes minimize the influence of size on the microstructural arrangement. The capability of system for autonomous microstructure development is further enhanced by activation of the nucleation mechanism as described by Eq. (3).

Anisotropic αβ and/or αδ interfaces

In forthcoming simulation studies, the main focus is on variation of $\zeta_{\alpha\beta}$ and/or $\zeta_{\alpha\delta}$ as the anisotropy strengths, based on Eq. (A2). Other system and process parameters are summarized in Table 3 of Appendix B. Simulations in this section are continued up to 150×10^6 time steps using 192 CPUs, with each simulation taking approximately 10 days. In Fig. 2(a), the evolved pattern for the isotropic configuration ($\zeta_{\alpha\beta} = \zeta_{\alpha\delta} = \zeta_{\beta\delta} = 0$) is shown. The growth direction is from left to right, with the red phase on the far-right side representing the liquid phase. Boundary conditions are periodic in the directions perpendicular to the growth direction, Neumann in the boundary in contact with the initial solid phases and Dirichlet in the right-side boundary to mimic infinite liquid flow. The coloring of the microstructure, delineates concentration of Bi in mol-% in the involved phases. This leads to illustration of α in yellow, β in blue and δ in magenta, respectively. In the magnified area a_1, the initial stage of the solid seeds is shown. At a later timestep, one α lamella nucleates between two β and δ lamellae diffusion driven, as highlighted in a_2. This nucleation and the subsequent stable growth of the α lamella significantly influence the final phase arrangement, leading to the formation of seven αβαδ-motifs. This means,

the free evolution of the floating grains under the given simulation conditions closely matches the experimentally observed phase arrangement [15] for this grain type.

Next, the anisotropy is activated in αβ phase boundaries with a set strength value of 0.025 (green-filled squares in the interfacial energy plots in Fig. 9). The evolved microstructure is shown in Fig. 2(b). The magnified area b_1 highlights an intermediate perturbation in this phase-growth procedure. As observed, such a perturbation causes local tilting of the solidified phases, which generally vanish in the further evolution process. The simulation ends with the formation of seven αβαδ-motifs in these quasi-isotropic grains. Despite the similarity of the formed grains to isotropic grains, the disturbances during the evolution process are stronger than those in the isotropic simulation. It appears that anisotropy initially influences the evolving pattern, but ultimately fails to cause a different phase arrangement in the microstructure, possibly due to the dominant diffusion and insufficient anisotropy strength. To further inspect, additional simulations are conducted with increased anisotropy strength. The results for some exemplary configurations configurations are shown in Fig. 3, which includes two sub-figures: (a) representing the αβ anisotropic case and (b) illustrating the αδ anisotropic case. In the study of αδ anisotropy, a similar approach is carried out, where $\zeta_{\alpha\beta} = \zeta_{\beta\delta} = 0$ and $\zeta_{\alpha\delta}$ is varied based on the values depicted in Fig. 2(a). The growth directions in illustrations of Fig. 3 are from bottom to top. The remarkable phenomena in the growth process, which mainly affect the final microstructures, are magnified below each sub-figure. In sub-figure (a), where $\zeta_{\alpha\beta}$ is varied by amounts of 0.05, 0.10, and 0.15, a_1 shows the nucleation of an α lamella leading to the formation of an αβαδ-motif. a_2 depicts the growth of two neighboring αδ bilayers. Although one of these δ lamellae is eliminated in later steps, the next δ layer grows stably to form a final $[\alpha\beta]_1[\alpha\delta]_2$ stacking sequence. A sharp elimination of the β phase takes place in a_3 as another effect of the αβ boundary anisotropy. This also leads to formation of the second $[\alpha\beta]_1[\alpha\delta]_2$ stacking sequence in this simulation. These motifs are magnified by cyan rectangles on top of the micrograph and are one of the experimentally detected superstructures, as discussed previously. In segment a_4 (with $\zeta_{\alpha\beta} = 0.1$), a β lamella is eliminated due to the

Figure 2 Evolved microstructures in DS studies of Bi-In-Sn system in **a** isotropic and **b** $\zeta_{\alpha\beta} = 0.025$ cases. Panel a_1 shows the initial Voronoi filling of solid phases and the primary growth state. Panel a_2 illustrates the nucleation and growth of an α lamella between the β and δ layers. Panel b_1 shows the intermediate instabilities caused by anisotropic interfaces..
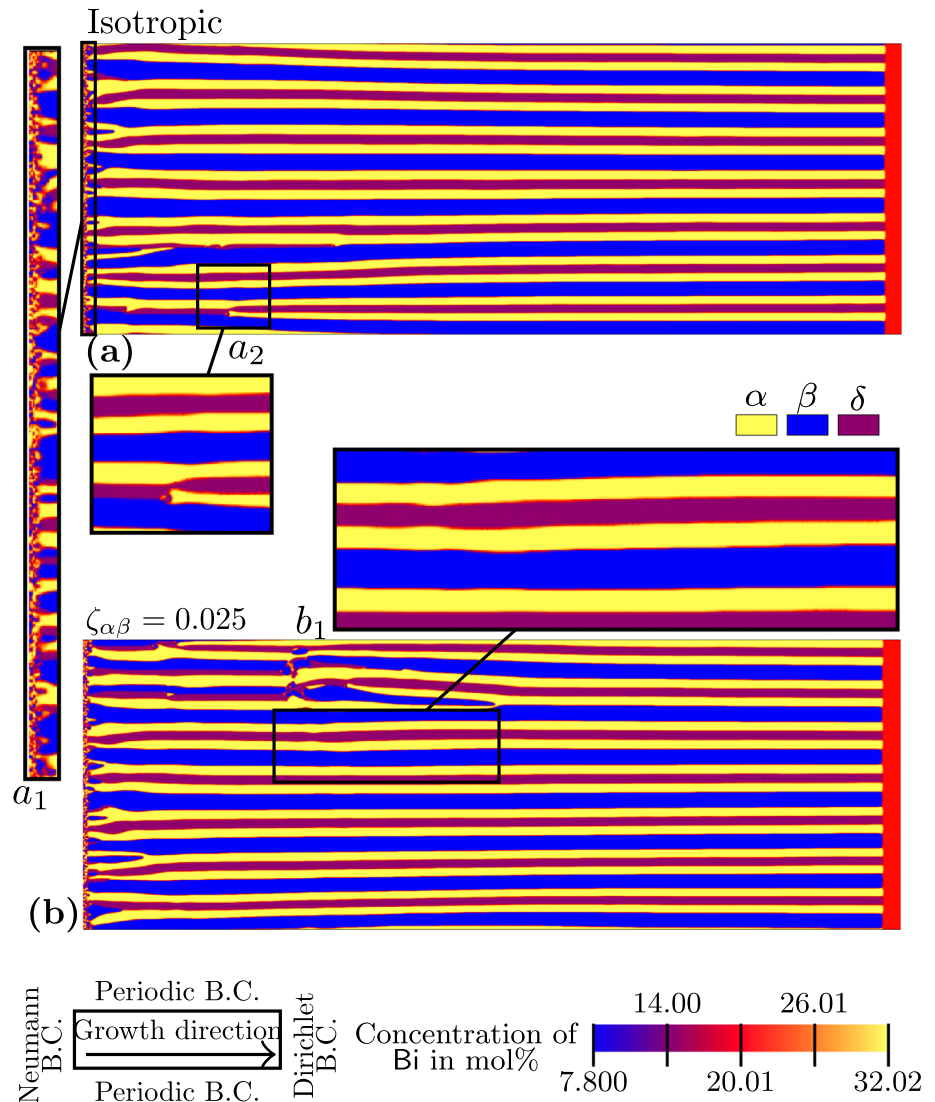
nucleation and stable growth of a δ seed at the β-liquid interface. This elimination-nucleation process results in the formation of an $[\alpha\beta]_2[\alpha\delta]_2$ motif, which is ultimately observed to be the widest formed superstructure in current article. The process can be considered analogous to experimentally reported recovery mechanism, *phase exchange* [10], (β-to-δ). It is important to note that these mechanisms are inherently three-dimensional (see Fig. 8 of [10] as an example); hence, the current two-dimensional simulation setup may not fully resolve all aspects of the underlying physical phenomena. However, it still retains key physical characteristics and provides valuable insights into the ongoing mechanisms, as will be discussed later. In addition, reducing the simulation dimension from 3D to 2D significantly

lowers computational costs in terms of both processing power and time. In the magnified section a_5, another β-to-δ phase-exchange occurs, resulting in the formation of an $[\alpha\beta]_1[\alpha\delta]_2$ motif. The sharp edges formed between α and β phases in a_6 are the next mentioned influence of anisotropic $\alpha\beta$ interface modeling. a_7 shows stable growth of two neighbouring $\alpha\delta$ bilayers from the initial simulation steps, resulting in the formation of an $[\alpha\beta]_1[\alpha\delta]_2$ sequence. To summarize the evolved patterns, $[\alpha\beta]_1[\alpha\delta]_2$, $[\alpha\beta]_2[\alpha\delta]_2$ and $\beta\alpha\delta$ are the observed additional motifs in locked grains evolving alongside the quasi-isotropic $\alpha\beta\alpha\delta$ units, when only $\alpha\beta$ interfaces are modeled anisotropically.

The depicted micrographs in Fig. 3(b) show exemplary simulation results in which $\zeta_{\alpha\beta} = \zeta_{\beta\delta} = 0$
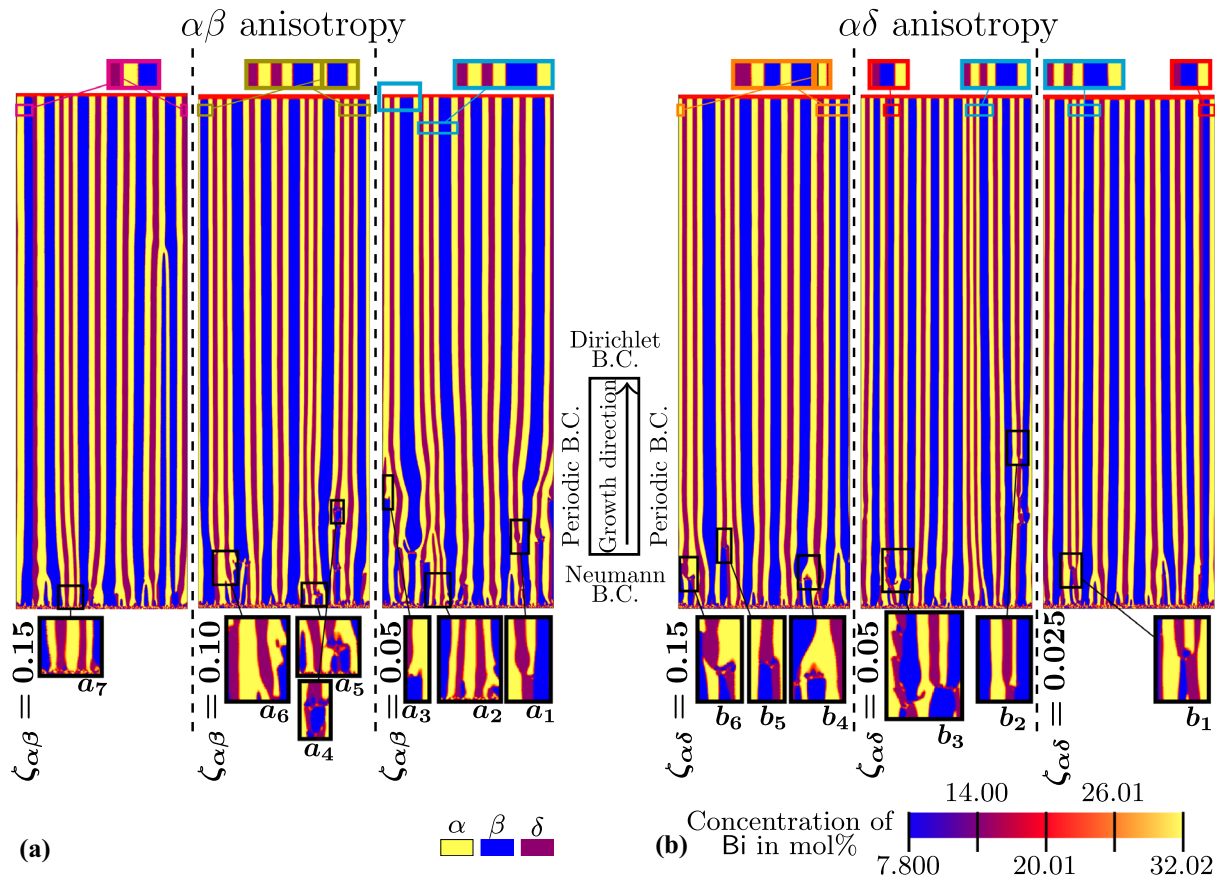
Figure 3 Evolved microstructures considering **a** $\alpha\beta$ anisotropic interfaces ($\zeta_{\alpha\delta} = \zeta_{\beta\delta} = 0$) and **b** $\alpha\delta$ anisotropic interfaces ($\zeta_{\alpha\beta} = \zeta_{\beta\delta} = 0$). The magnifications below each sub-figure highlight the occurred instability/mechanism in the growth procedure. The finally resulted motifs in the locked grains are underscored in the expanded views above each sub-figure..

and $\zeta_{\alpha\delta} \in \{0.025, 0.05, 0.15\}$. In b_1, the nucleation of α and δ phases at the β-liquid interface leads to a 2D lamella branching, resulting in the formation of an $[\alpha\beta]_1[\alpha\delta]_2$ motif, which continues to grow stably until the end of the simulation. In b_2, the nucleation and growth of an α layer between the β and δ layers occurs, similar to the previously described cases. In the enlarged view b_3, the formation of an unstable sawtooth structure occurs as a result of continuous nucleation and dissolution of the δ phase, influenced by anisotropic $\alpha\delta$ interfaces. This sawtooth pattern, also observed experimentally [15], does not persist in later simulation steps. Instead, the δ lamella evolves into a stable structure with predominantly flat phase boundaries. In anisotropic modeling of the $\alpha\delta$ interface, the sharp elimination of the β phase takes place only if $\zeta_{\alpha\delta} \geqslant 0.15$. The magnified segment b_4 shows such a case. b_5 and b_6 magnify β-to-δ and α-

to-δ phase exchanges observed with $\zeta_{\alpha\delta} = 0.15$. The evolved superstructures in Fig. 3(b) are $[\alpha\beta]_1[\alpha\delta]_2$, $[\alpha\beta]_2[\alpha\delta]_1$ and $\alpha\beta\delta$, highlighted by cyan, orange, and red rectangles, respectively. The maximum achievable values for $\alpha\beta$ and $\alpha\delta$ anisotropy strengths are $\zeta_{\alpha\beta}^{max} = 0.25$ and $\zeta_{\alpha\delta}^{max} = 0.45$. Going beyond these thresholds leads to a loss of stability, ultimately causing the simulations to fail.

In further simulation studies, $\alpha\beta$ and $\alpha\delta$ anisotropies are activated simultaneously. As a brief indication, no new patterns emerge beyond those observed in the individual anisotropic configurations. The previously identified units and mechanisms, such as $\alpha\beta\delta$, $[\alpha\beta]_2[\alpha\delta]_1$, $[\alpha\beta]_1[\alpha\delta]_2$, $[\alpha\beta]_2[\alpha\delta]_2$, β-to-δ and β-to-α phase exchanges, and sharp β-layer elimination in various anisotropy configurations, remain representative. The type and quantity of these instabilities are discussed in detail in the next section.
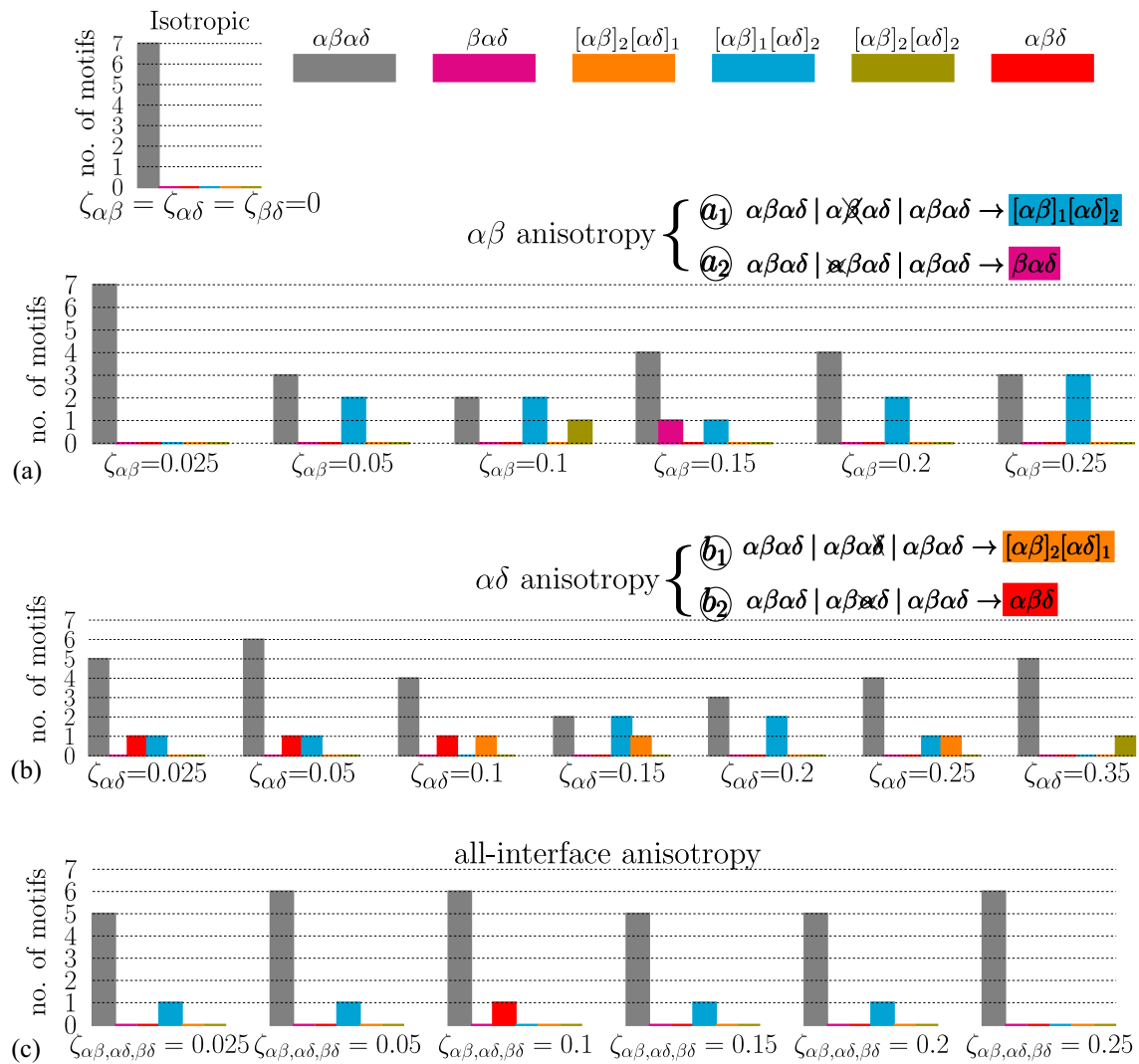
Figure 4 Summary of the observed patterns in **a** $\alpha\beta$-interface anisotropy ($\zeta_{\alpha\delta} = \zeta_{\beta\delta} = 0$), **b** $\alpha\delta$-interface anisotropy ($\zeta_{\alpha\beta} = \zeta_{\beta\delta} = 0$) and **c** activated anisotropy in all interfaces.

Evolved patterns and explanatory morphology map

To facilitate the analysis of the evolved patterns, a summary of all observed motifs from section 3.2.1 is presented and quantified in Fig. 4 in the form of bar charts. The seven $\alpha\beta\alpha\delta$ motifs that emerge in the isotropic case are represented by a single gray-colored bar in the top-left of the figure. Figure 4(a) illustrates the results for anisotropically modeled $\alpha\beta$ interfaces. As anisotropy increases, the number of formed quasi-isotropic grains decreases from seven to four, three, and two, depending on the applied anisotropy strength. However, this decrease is not linearly proportional to variation in $\zeta_{\alpha\beta}$ across these

simulations. $[\alpha\beta]_1[\alpha\delta]_2$ is the most frequently formed superstructure in this configuration, depicted in cyan. $[\alpha\beta]_2[\alpha\delta]_2$ and $\beta\alpha\delta$ also emerge, corresponding to $\zeta_{\alpha\beta} = 0.1$ and $\zeta_{\alpha\beta} = 0.15$, in that order. To explain the resultant phase arrangements, @₁ and @₂ schematics assume three hypothetical $\alpha\beta\alpha\delta$ repeat units. This representation is based on the assumption that the system naturally favors the formation of $\alpha\beta\alpha\delta$ motifs, but $\alpha\beta$ interface anisotropy can lead to the elimination of either α or β lamellae within $\alpha\beta$ bilayers. In @₁, the omission of a β lamella is considered, whereas in @₂, an α-lamella is omitted following this assumption. As a consequence, the resultant $[\alpha\beta]_1[\alpha\delta]_2$ and $\beta\alpha\delta$

motifs, represented by cyan and pink bars, align well with the structures observed in the simulation results.

In Fig. 4(b), a similar illustration is provided for the observed patterns in simulations with anisotropically modeled $\alpha\delta$ interfaces. Two new motifs, $\alpha\beta\delta$ and $[\alpha\beta]_2[\alpha\delta]_1$, appear, represented by red and orange bars, respectively. It is also observed that $[\alpha\beta]_2[\alpha\delta]_2$, as the widest superstructure, is formed in a higher anisotropy strength, compared to the anisotropic $\alpha\beta$ cases. Schematics ⓑ₁ and ⓑ₂ are structured using the same logic as ⓐ₁ and ⓐ₂, but with the assumption that anisotropy at the $\alpha\delta$ interface leads to the elimination of either α or δ lamellae in an $\alpha\delta$ bilayer. Consequently, $[\alpha\beta]_2[\alpha\delta]_1$ and $\alpha\beta\delta$ emerge as the expected morphological patterns, aligning well with the simulation results. Nevertheless, similar to Fig. 4(a), a stepwise reduction in $\alpha\beta\alpha\delta$ units or a proportional increase in the number of formed superstructures with $\zeta_{\alpha\delta}$ increase is not observed. This persistent inconvenience in current DS simulation results necessitates further investigation.

Figure 4(c) presents the results for fully anisotropic interfaces. Notably, quasi-isotropic grains remain dominant, giving the impression of similarity to the isotropic simulation. Additionally, the number of formed instabilities is lower than what may be expected. Realizing the underlying mechanism responsible for this behavior demands additional investigations. Furthermore, by examining all three sub-figures, $[\alpha\beta]_1[\alpha\delta]_2$ emerges as the most frequently formed superstructure, which is primarily captured by ⓐ₁ in our schematics. This prevalence further motivates additional investigations into its underlying causes. While the dominant influence of $\alpha\beta$ interface anisotropy explains the formation of $[\alpha\beta]_1[\alpha\delta]_2$ in Fig. 4(c), its consistent presence in Fig. 4(b) is unexplained by the introduced lamellae-elimination-based morphology map. These *Observations* (denoted as *Ob*) derived from the DS simulations are summarized below:

*Ob*1   When all interfaces are modeled anisotropically, quasi-isotropic grains appear more frequently than in cases with only $\alpha\beta$ or $\alpha\delta$ interface anisotropy.

*Ob*2   Despite a linear increase in anisotropy strength-whether in the $\alpha\beta$ or $\alpha\delta$ interfaces- a proportional increase in the number of formed superstructures or a systematic suppression of quasi-isotropic $\alpha\beta\alpha\delta$ motifs is not observed in current domain size. Instead, anisotropy affects the microstructure in current DS simulations in a primarily qualitative manner, guiding the morphological evolution and stability of motifs without establishing a direct quantitative correlation.

*Ob*3 $[\alpha\beta]_1[\alpha\delta]_2$ is the most commonly observed superstructure in performed simulations. According to our classification, it is expected to form predominantly in $\alpha\beta$ anisotropies.

The final discussion in this section focuses on the possible combinations of the assumed elimination mechanisms. In Table 1, the potential combinations of ⓐ₁, ⓐ₂, ⓑ₁ and ⓑ₂ are listed, along with the resultant patterns for each case. Theoretically, eleven distinct combinations can be considered using these four cases. In each row of table, the cases that lead to the same phase arrangement are grouped together and separated by commas. According to the first row, a significant number of anisotropy combinations can result in quasi-isotropic grains. Although these gains closely resemble the $\alpha\beta\alpha\delta$ motif in floating grains, a fundamental difference in their formation process can be inferred. This occurs due to the reduction of the three hypothetical $\alpha\beta\alpha\delta$ repeat units to two which is served as a preliminary explanation for *Ob*1. From the second and third rows of the table, it is evident that $[\alpha\beta]_2[\alpha\delta]_1$ occurs exclusively when anisotropy is primarily present at $\alpha\delta$ phase boundaries, while $[\alpha\beta]_1[\alpha\delta]_2$ forms in purely anisotropic $\alpha\beta$ interfaces or in cases where $\alpha\beta$ anisotropy is combined with $\alpha\delta$ boundary anisotropy. These insights may explain the presence of orange bars only in Fig. 4(b), but the mechanism behind *Ob*3 still remains unresolved.

The fourth and fifth rows of Table 1 predict the formation of single β lamellae and $\beta\delta$ bilayers. These cases have not been observed in the present DS simulations. However, in experimental studies [9], single β lamellae have been reported as segments in $[\alpha\beta]_4[\alpha\delta]_6\beta$ superstructures. Similarly, $\beta\delta$ bilayers have been documented, albeit as rare occurrences in

Table 1 Combination of different anisotropy-related phase-elimination mechanisms, $\textcircled{a}_1$, $\textcircled{a}_2$, $\textcircled{b}_1$, $\textcircled{b}_2$ and their resultant phase arrangements

	combination	resultant pattern
1	$\textcircled{a}_1\textcircled{b}_1$, $\textcircled{a}_1\textcircled{a}_2\textcircled{b}_1$, $\textcircled{a}_1\textcircled{a}_2\textcircled{b}_2$, $\textcircled{a}_1\textcircled{b}_1\textcircled{b}_2$, $\textcircled{a}_1\textcircled{a}_2\textcircled{b}_1\textcircled{b}_2$	$\alpha\beta\alpha\delta\|\alpha\beta\alpha\delta\|\alpha\beta\alpha\delta \Longrightarrow$ $\alpha\beta\alpha\delta\|\alpha\beta\alpha\delta$
2	$\textcircled{a}_1\textcircled{a}_2$, $\textcircled{a}_1\textcircled{b}_2$	$[\alpha\beta]_1[\alpha\delta]_2$
3	$\textcircled{b}_1\textcircled{b}_2$	$[\alpha\beta]_2[\alpha\delta]_1$
4	$\textcircled{a}_2\textcircled{b}_1$, $\textcircled{a}_2\textcircled{b}_1\textcircled{b}_2$	single β lamella
5	$\textcircled{a}_2\textcircled{b}_2$	$\beta\delta$ bilayer

confined domains. Thus, these phenomena can be interpreted as effects of anisotropic interfaces within the proposed morphology map.

Given the observed local inclinations in the solidified phases due to anisotropy-induced instabilities, RDS simulations may provide additional insights. This expectation is due to possibility for a quantitative characterization of tilted growth, as demonstrated in [15–17, 21]. A detailed investigation is presented in the upcoming sections.

RDS simulations of the Bi-In-Sn system

Similar to the DS cases, the forthcoming RDS investigations extend the established system in [21], where $\zeta_{\alpha\beta}$ and/or $\zeta_{\alpha\delta}$ are systematically varied. All other model and process parameters remain unchanged as outlined in mentioned reference, with key details summarized as follows: The simulation domain consists of 965×965 cells, corresponding to 301.8×301.8 μm. The initial square domain is bounded by two barriers, forming an annular phase-evolution region with inner and outer radii, denoted by r_i and r_o. The rotation center, Ω, serves as the reference point for measuring trajectory radii within the solidified phases. The initial solid-phase filling consists of five lamellae arranged in an $\alpha\beta\alpha\delta$ sequence in both growth and melting fronts.

The impact of anisotropic interfaces on trajectory radii in the solidified phases is examined in this case study. To minimize potential boundary effects (see [21]), an α lamella with radius $r \simeq (r_i + r_o)/2$ is selected. This lamella, hatched in the illustrated micrographs, forms distinct interfaces with two β and δ lamellae, whose evolving profiles are analyzed below. Fig. 5(a-c) presents the resultant microstructures for the isotropic case, along with exemplary anisotropic cases of $\zeta_{\alpha\beta} = 0.1$ and $\zeta_{\alpha\delta} = 0.15$. Each micrograph is accompanied by a plot showing the variation of $\alpha\beta$ and/or $\alpha\delta$ boundary radii, $r_{\alpha\beta}$ and $r_{\alpha\delta}$,

with respect to the rotational angle θ. In Fig. 5(a), an almost linear dependency is observed, with oscillations in the solidified phase boundaries occurring within the rotational range $90° \leqslant \theta \leqslant 135°$. These oscillations, due to intermediate evolution stages, vanish with continued simulation. In the anisotropic cases Fig. 5(b, c), inclined growth of the solidified phases is visually evident. The radius profiles exhibit multimodal behavior with multiple peaks and valleys. Despite local minima, an overall increase in radii is observed. Critical points marking local extrema appear approximately every 45°, maintaining a periodic pattern. This periodicity manifests in a U-shaped pattern within the first 90° of rotation. Despite oscillations in $90° \leqslant \theta \leqslant 135°$, the general shape remains periodic in further simulation steps. This consistency in $r - \theta$ plots suggests that further RDS simulations can be limited to a quarter rotation, significantly reducing computational costs.

Figure 5(d) presents two schematics based on observed $r - \theta$ dependencies. The linear radius increase in the isotropic case is termed *straight spiral growth*, indicating a linear transformation of the solidifying lamella shape from circular to spiral. In isotropic simulation, the radius increase (up to 10% at $\theta = 360°$) is notably smaller than in experiments [15], likely due to better alignment between the disk center and the high-temperature-gradient area in simulations (see Fig. 5 in [21]). Meanwhile, the radius change in locked grains exhibits what is referred to as *tilted spiral growth*. The inclined growth in solidification process of locked grains is clearly observed here. Figure 6 shows the evolved microstructures after $\pi/2$ rad rotation under isotropic and anisotropic conditions. The initial $\alpha\beta\alpha\delta$ sequences are magnified on the left side. Sub-figures (b-e) illustrate anisotropic $\alpha\beta$ interfaces, while (f–j) show anisotropic $\alpha\delta$ results.

By considering $\alpha\beta\alpha\delta$ motifs as coupled combinations of $\alpha\beta$ and $\alpha\delta$ bilayers, we observe that in $\alpha\beta$ anisotropic cases, the system tends to eliminate α
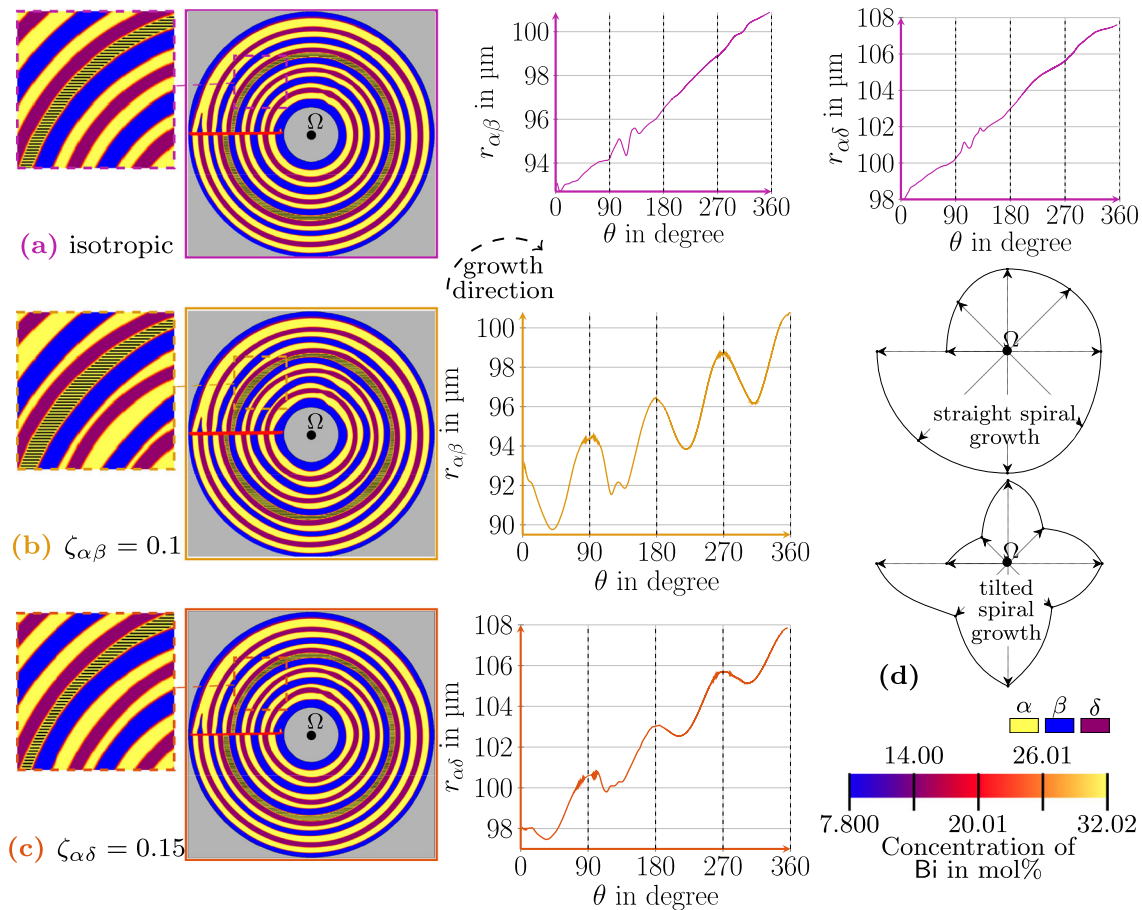
Figure 5 Variation of rotation radii in hatched lamellae, **a** Isotropic simulation presented in [21], **b** $\alpha\beta$ interface anisotropy with strength of 0.1, **c** $\alpha\delta$ anisotropy with strength of 0.15. **d** schematic illustrations of straight and tilted growths in floating and locked grains..

lamellae in $\alpha\beta$ bilayers. These lamellae become thinner in Fig. 6(b), leading to their first elimination at $\zeta_{\alpha\beta} = 0.15$, as shown in sub-figure (c). The corresponding rotational angle for this elimination is $\theta \simeq 30°$. Consequently, in Sub-figure (d), phase elimination occurs at a slightly lower θ value of 26°. This behavior provides evidence for the assumed mechanism ⓐ₂ and supports the prediction of $\beta\alpha\delta$ motif formation in Sect. 3.2.2. In higher $\alpha\beta$ anisotropy strengths, the elimination trend continues, and the number of eliminated α lamellae reaches its final count of three in these simulation series.

The resultant microstructures in Fig. 6(f–j) show the influence of $\alpha\delta$ anisotropy on α lamellae in $\alpha\delta$ bilayers. This observation aligns well with the introduced mechanism ⓑ₂ in Sect. 3.2.2, leading to the formation of $\alpha\beta\delta$ motifs. The α lamellae in $\alpha\delta$ bilayers become thinner as $\alpha\delta$ anisotropy is activated. The stepwise increase of $\zeta_{\alpha\delta}$ strengthens this mechanism.

The first $\alpha\beta\delta$ motif is observed at an anisotropy strength of $\zeta_{\alpha\delta} = 0.35$, which is higher compared to the similar case in $\alpha\beta$ anisotropy. This indicates that a stronger $\alpha\delta$ anisotropy is required for a significant pattern change in solidification simulations of the Bi-In-Sn system. The observations in Fig. 6 indicate that, unlike the DS results, in RDS simulations, the intensity of the assumed lamella-elimination mechanisms increases proportionally with the strength of anisotropy. This is clearly evident due to the possibility of ordered initial solid-phase filling in these simulations, which is difficult to capture in DS configurations. Hence, an explanation for *Ob*2 is derived.

The variation of $r_{\alpha\beta}$ and $r_{\alpha\delta}$ with respect to the rotational angles in all anisotropic scenarios is analyzed in Fig. 7. Sub-figure (a) represents the $\alpha\beta$ anisotropy, while sub-figure (b) presents the $\alpha\delta$ anisotropy results. In each case, the variations for both interfaces are plotted to observe their reciprocal
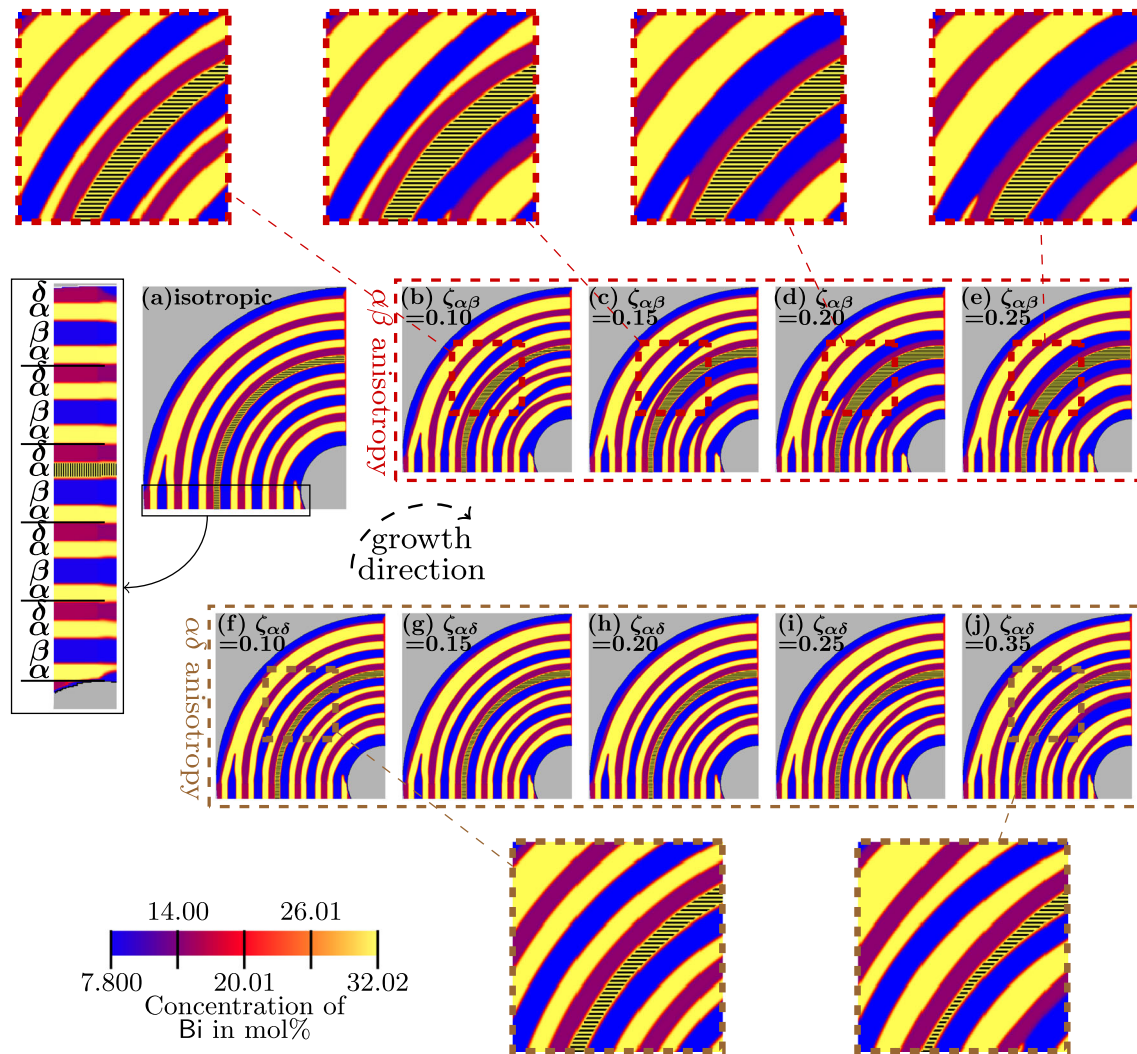
Figure 6 Evolved microstructures after $\pi/2$ rad rotation. **a** isotropic simulation, **b**–**e** $\alpha\beta$ interface anisotropy and **f**–**j** $\alpha\delta$ interface anisotropy. Hatched areas are the selected α lamellae to measure $r_{\alpha\beta}$ and $r_{\alpha\delta}$ in Fig. 7..

effect on the inclined growth of the solidified phases. The formed pattern in each case remains nearly constant as the anisotropy strength increases, except for the pattern change in the $r - \theta$ plot when $\zeta_{\alpha\beta} \geq 0.2$. This behavior is attributed to the influence of three eliminated α lamellae in $\alpha\beta$ bilayers on the measured radii. Additionally, even at $\zeta_{\alpha\beta} = 0.25$, the new pattern remains almost unchanged.

Another conclusion is that activation of anisotropy in any interface affects neighboring interfaces, in accordance to experimental observations [15, 46]. In simulations this happens even if the neighbouring interface is modeled isotropically. In this scenario, the expected U-shaped patterns in anisotropic interfaces also appear in nearby isotropic phase boundaries. This reciprocal interface effect could serve as an

additional factor in the occurrence of the combined mechanisms listed in Table 1. However, further investigations are required to confirm this conclusion.

The final study in this article focuses on RDS simulations with active anisotropies in both $\alpha\beta$ and $\alpha\delta$ interfaces. The investigations aim to explore additional explanations for *Ob*1 regarding the simultaneous activation of anisotropies in all phase boundaries. One such simulation in [21] involves setting $\zeta_{\alpha\beta}$ and $\zeta_{\alpha\delta}$ to an equal value of 0.15. It is shown that this configuration leads to more pronounced inclined growth in $\alpha\beta$ interfaces compared to $\alpha\delta$ interfaces (see Fig. 7 of [21]). Given the stable rotational growth in the solidified phases, this condition is chosen as the baseline for subsequent investigations. In this

Figure 7 Variation of $\alpha\beta$ and $\alpha\delta$ interface radii with respect to the rotational angle θ, **a** $\alpha\beta$ interface anisotropy and **b** $\alpha\delta$ interface anisotropy. The radii measurements are performed based on the hatched α lamellae in Fig. 6..
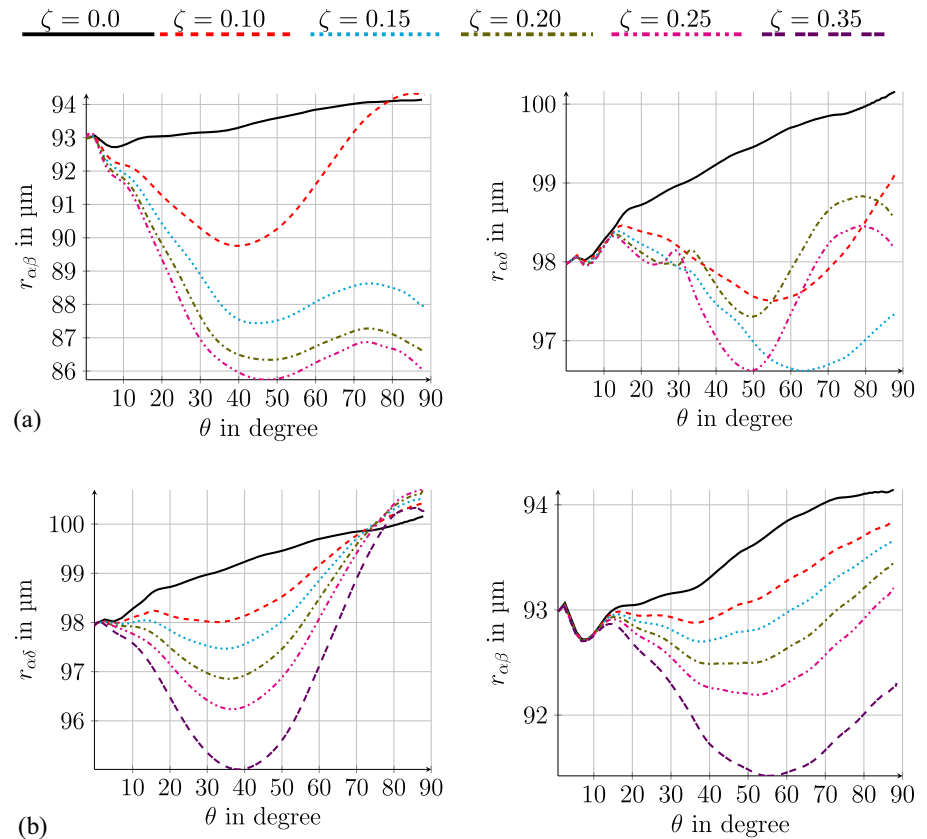
context, the ratio of anisotropy strengths κ is defined as $\kappa = \zeta_{\alpha\delta}/\zeta_{\alpha\beta}$. Thus, $\kappa = 1$ represents the baseline configuration. While keeping $\zeta_{\alpha\beta}$ constant at 0.15, $\zeta_{\alpha\delta}$ is increased up to 0.45, i.e., $\kappa \in \{1, 2, 3\}$. The resulting microstructures are shown in Fig. 8.

The radii measurements are performed in the hatched lamellae, similar to the previous cases. Micrographs suggest that activating anisotropy in all interfaces induces simultaneous tilting of the solidified lamellae, preventing phase elimination in RDS simulations. Under these conditions, phase boundaries remain inclined yet closer to parallel compared to individual $\alpha\beta$ or $\alpha\delta$ anisotropic cases. The intensity of parallelism of interfaces can be studied by comparing $dr_{\alpha\beta}/d\theta$ and $dr_{\alpha\delta}/d\theta$ during the evolution process. The plot in Fig. 8 illustrates these derivatives. Black, cyan and red lines correspond to $\kappa = 1, 2$ and 3, respectively. Solid lines represent $\alpha\beta$ interfaces, while dashed lines denote $\alpha\delta$ interfaces. It is observed that with increasing κ, the deviation between dashed and solid lines significantly decreases. It can be said that another explanation for $Ob1$ is achieved: when all interfaces are modeled anisotropically, simultaneous tilting of neighboring

interfaces can prevent phase elimination. In other words, these anisotropies do not negate each other but instead could interact to inhibit superstructure formation, unlike single $\alpha\beta$ or $\alpha\delta$ anisotropies.

Summary

This study utilizes a grand-potential-based phase-field model in which interfacial energy anisotropy is modeled by a cubic function. To explain experimentally observed eutectic solidification patterns in ternary systems, simulations are conducted for NiAl-10Mo and Bi-In-Sn systems. In DS simulations, anisotropic interfaces are shown to influence fiber morphology in NiAl-10Mo, leading to cuboid rather than cylindrical fibers. The DS setup also reveals the formation of $\alpha\beta\alpha\delta$ repeat units in isotropic or quasi-isotropic grains of Bi-In-Sn and additional motifs in locked grains as $[\alpha\beta]_1[\alpha\delta]_2$, $[\alpha\beta]_2[\alpha\delta]_1$, $[\alpha\beta]_2[\alpha\delta]_2$, $\beta\alpha\delta$ and $\alpha\beta\delta$. During the transitional phase evolution, diverse irregularities emerge, such as the sharp removal of lamellae, phase exchange, lamella branching, and the development of sawtooth

Figure 8 Evolved microstructures for different κ values whereas $\zeta_{\alpha\beta} = 0.15$. The variation of $dr/d\theta$ is plotted for each case considering both $\alpha\beta$ and $\alpha\delta$ interfaces..
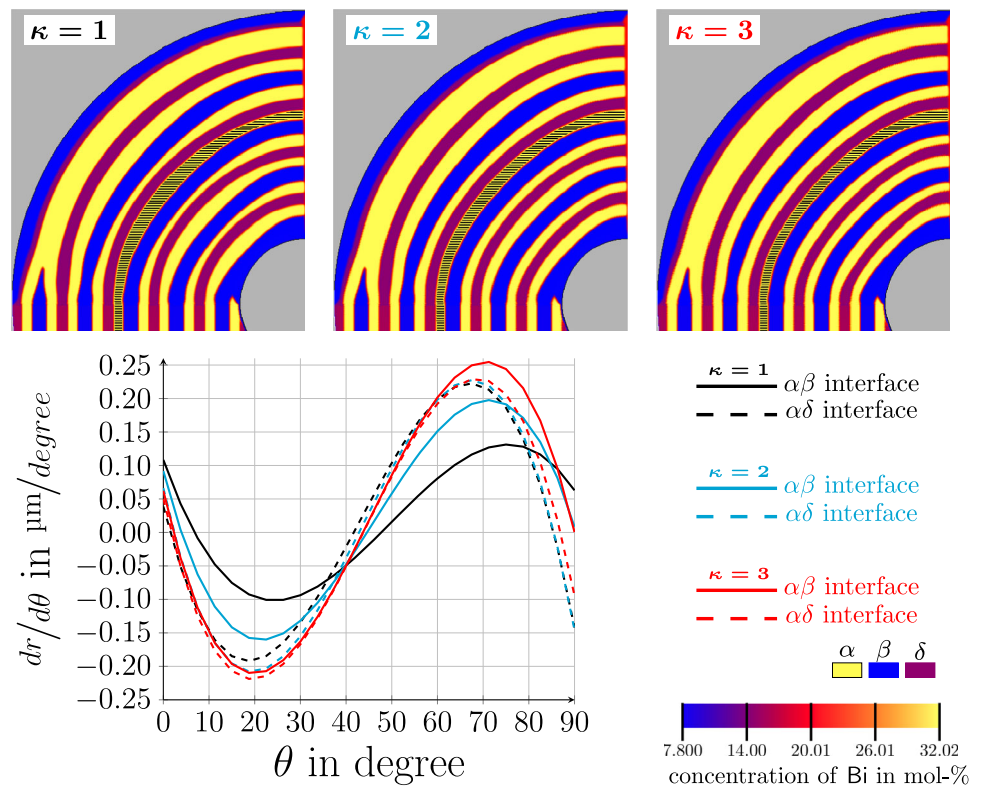
patterns. In order to explain the formation cause behind the superstructures, a morphology map is introduced mainly based on the phase-elimination possibility due to the anisotropic interfaces. The approach effectively explains the primary causes of superstructure formation in simulations and accounts for certain experimentally observed phenomena, such as single β lamellae and $\beta\delta$ bilayer formations, which are absent in our results. While the performed analyses show promising capabilities, further validation under differing process conditions is necessary to assess its robustness and potential refinements.

Outlook

*Ob*3 concerning the persistent presence of $[\alpha\beta]_1[\alpha\delta]_2$ motifs under any anisotropic condition remains the subject of future research. To gain further insights, additional RDS simulations will be performed using larger simulation domains with Voronoi tessellation of the initial solid seeds. In this setup, evidence for $\textcircled{a_1}$ and $\textcircled{b_1}$ mechanisms are expected to emerge. Since these mechanisms rely on the elimination of the β and δ phases, they are unlikely to occur under the current

RDS configuration, where the filled phases with robust bulks create extreme resistance against these eliminations. However, introducing a Voronoi tessellation with an active nucleation mechanism removes this constraint. Another promising research direction involves investigating the effect of anisotropy angle rotation. In the current configuration, the anisotropy rotational angle (α_{ij} in [47]) is fixed at zero. Given the reciprocal interface effect discussed earlier, allowing rotational anisotropy provides deeper insights into the underlying mechanisms. Future works will explore extensions of the modelling framework to account for the simultaneous growth of floating and locked grains, as well as dynamic variations in process parameters such as solidification velocity [45]. Additionally, system parameters like anisotropy strength are to be varied dynamically to analyze their impact on microstructure evolution. The anisotropy formulation can be varied for example in an ellipse shape [17]. Simulations of these anisotropy types are objectives for future works.

Mohagheghi and Şerefoğlu have introduced a new class of eutectic grains, termed Laminated Matrix with Rods LMR by their recent RDS experiments [48].

Table 2 NiAl-10Mo system, L: Liquid, F: Fiber and M: Matrix phases. $G(c_{Al}, c_{Mo}, T) = A_1(T) \cdot c_{Al}^2 + A_2(T) \cdot c_{Mo}^2 + A_3(T) \cdot c_{Al} \cdot c_{Mo} + A_4(T) \cdot c_{Al} + A_5(T) \cdot c_{Mo} + A_6(T)$ (from [56])

Phase name	Gibbs energy approximation parameters				
Fiber	$A_1(T) = -3054.022T + 8548519.30$		$A_2(T) = -11806.786T + 24817509.4$		
	$A_3(T) = -15955.736T + 35269065.2$		$A_4(T) = 15252.910T - 33974178.4$		
	$A_5(T) = 23020.250T - 48460728.9$		$A_6(T) = -11292.974T + 23688082$		
Matrix	$A_1(T) = -1300.426T + 2902628.20$		$A_2(T) = -7970.744T + 17433820.7$		
	$A_3(T) = -102.330T + 622785.006$		$A_4(T) = 1449.528T - 3185144.56$		
	$A_5(T) = 116.916T - 385991.425$		$A_6(T) = -476.573T + 850980.846$		
Liquid	$A_1(T) = -138.250T + 430879.432$		$A_2(T) = -945.677T + 1821352.34$		
	$A_3(T) = -274.839T + 642835.112$		$A_4(T) = 294.671T - 723028.985$		
	$A_5(T) = 357.285T - 684080.383$		$A_6(T) = -209.938T + 276459.004$		

Parameter	Simulation value	Physical value	Parameter	Simulation value	Physical value
dt	0.02, 0.06	$4, 12 \cdot 10^{-9}$s	$T_{eut.}$	1.0	$1875.47K$
D_L	3.68	$10^{-9} rmm^2 s^{-1}$ [57]	ζ_{MF}	0.066	–
D_M, D_F	0	0	τ_{MF}, τ_{FM}	8.5	calculated
γ_{0MF}	$8.84 \cdot 10^{-3}$	0.65 Jm^{-2}	τ_{ML}, τ_{LM}	0.00168	from
γ_{ML}	$8.84 \cdot 10^{-3}$	0.65 Jm^{-2}	τ_{FL}, τ_{LF}	0.094	[32]
γ_{FL}	$8.84 \cdot 10^{-3}$	0.65 Jm^{-2}	G^{DS}	$1.31 \cdot 10^{-7}$	33.4 Kmm^{-1} [5]
γ_{MFL}	$15 \cdot \gamma_{\alpha\beta}$	–	ε	4.0	29.48 nm
dx	1.0, 2.0	0.00737, 0.00368 μm			

Eutectic composition

Phase name	c_{Al} in mol-%	c_{Mo} in mol-%	c_{Ni} in mol-%
Fiber	8.64	91.2	0.16
Matrix	49.444	0.092	50.464
Liquid	43.9	9.4	46.7

These grains exhibit a fully 3D nature, characterized through double-sided microscopy. Their findings suggest that $\alpha\delta$ anisotropy leads to the formation of large δ-phase regions on one side of the sample, while the opposite side predominantly consists of α and β phases. Given the novelty of this topic, many open questions remain, necessitating further investigations. A particularly intriguing avenue for future research is extending the current 2D simulations to a fully 3D framework. This transition will provide valuable insights into the formation mechanisms of LMR and further refine our understanding of anisotropic effects in eutectic solidification.

Acknowledgements

Data Availability

All data supporting the findings of this study are fully included within the manuscript.

Declarations

Conflict of interest The authors declare that they have no conflict of interest.

Ethical approval Not Applicable.

Appendix A Anisotropy formulation and stability

The interfacial energy anisotropy is modeled via the anisotropy function $a_c(q_{\hat{\alpha}\hat{\beta}})$ [49] in the gradient energy density term in Eq. (1), expressed as:

$$a(\boldsymbol{\phi}, \nabla\boldsymbol{\phi}) = \sum_{\hat{\alpha}<\hat{\beta}} \gamma_{\hat{\alpha}\hat{\beta}} \Big(a_c(q_{\hat{\alpha}\hat{\beta}})\Big)^2 \Big|q_{\hat{\alpha}\hat{\beta}}\Big|^2,$$

$$a_c(q_{\hat{\alpha}\hat{\beta}}) = 1 - \zeta_{\hat{\alpha}\hat{\beta}}\left(3 - 4\frac{\Big|q_{\hat{\alpha}\hat{\beta}}\Big|_4^4}{\Big|q_{\hat{\alpha}\hat{\beta}}\Big|^4}\right). \tag{A1}$$

Here, the anisotropy function a_c depends on the generalized gradient vector of the phase fields,

$q_{\hat{\alpha}\hat{\beta}} = \phi_{\hat{\alpha}}\nabla\phi_{\hat{\beta}} - \phi_{\hat{\beta}}\nabla\phi_{\hat{\alpha}}$, and $\zeta_{\hat{\alpha}\hat{\beta}} > 0$ denotes the anisotropy strength, which introduces orientation dependence into the pattern formation [50]. The hat symbols distinguish phase identifiers from summation indices. Special norm operators $|\cdot|^4$ and $|\cdot|_4^4$ are defined in [49].

This spatial formulation in Eq. (A1) is directly implemented in the 3D simulations of the NiAl-10Mo system. For the 2D simulations of eutectic solidification in the Bi-In-Sn system, the formulation simplifies to a classical anisotropy expression:

$$\gamma_{\bar{\alpha}\bar{\beta}}(\theta) = \gamma_{0\bar{\alpha}\bar{\beta}}\Big(1 - \zeta_{\bar{\alpha}\bar{\beta}}\cos(4\theta)\Big), \tag{A2}$$

where $\bar{\alpha}$ and $\bar{\beta}$ represent two neighboring phases at an interface where anisotropy is applied. In the isotropic case, the interface energy values used are $\gamma_{0\alpha\beta} = \gamma_{0\beta\delta} = 9.26 \times 10^{-4}$ [-] and $\gamma_{0\alpha\delta} = 2.78 \times 10^{-4}$ [-], as listed in Table 3. These correspond to the physical values 0.29 Jm^{-2} and 0.087 Jm^{-2}, respectively.

Due to the use of Voronoi tessellation for initial nuclei, the β and δ phases may become adjacent during intermediate growth. In such cases, we assume $\zeta_{\beta\delta} = \zeta_{\alpha\beta}$. The effect of this anisotropy formulation on orientation-dependent energy is illustrated in Fig. 9(a) for different values of ζ.

This four-fold orientation-dependent energy form has a long-standing history in the phase-field community [51, 52]. As shown in Fig. 9(b), the Wulff plots for two sample values $\zeta_{\bar{\alpha}\bar{\beta}} = 0.10$ and 0.30 reveal cusp and facet formation, indicating directional interface instabilities [53]. The *interface stiffness*, defined as

$$S(\theta) = \gamma(\theta) + \gamma''(\theta),$$

can become negative for high anisotropy strengths, limiting permissible ζ values. As reported by Kobayashi [51], the critical value for maintaining positive stiffness in all directions is $\zeta_{cr} \approx 0.066$. In Fig. 9(b), angular intervals with negative stiffness are indicated with dotted shading, predicting interfacial instabilities or loss of certain orientations. In the 3D simulations of the NiAl-10Mo system, the value $\zeta_{MF} = 0.066$ is selected to avoid such instabilities. This value supports the stable evolution of cylindrical fibers into cuboidal morphologies. However, for the Bi-In-Sn system, we explore a wide range of anisotropy strengths ($\zeta \in [0.00, 0.45]$) to investigate its influence on the morphology of the eutectic growth front.

Table 3 LULC change transition matrix showcasing percentage wise area changes(AC) in each class. Bold values (No Change)

Phase name	Gibbs energy approximation parameters	
α	$A_1(T) = 3014.607T - 896340.473$	$A_2(T) = 7087.078T - 2189377.1803$
	$A_3(T) = 3296.242T - 929782.259$	$A_4(T) = -4116.795T + 1186641.527$
	$A_5(T) = -10523.232T + 3220675.0386$	$A_6(T) = 4106.939T - 1263269.831$
β	$A_1(T) = -143.363T + 55902.219$	$A_2(T) = 138.230T - 37075.096$
	$A_3(T) = 355.122T - 115506.027$	$A_4(T) = -255.378T + 78337.588$
	$A_5(T) = -198.487T + 51646.124$	$A_6(T) = 3.884T - 15477.151$
δ	$A_1(T) = -871.762T + 301469.411$	$A_2(T) = 122.777T - 26128.366$
	$A_3(T) = 348.878T - 139478.362$	$A_4(T) = 22.402T - 5281.841$
	$A_5(T) = -154.236T + 40925.907$	$A_6(T) = -30.836T - 6902.264$
Liquid	$A_1(T) = -13.421T + 13192.535$	$A_2(T) = 12.381T + 4229.506$
	$A_3(T) = 23.675T - 5488.634$	$A_4(T) = -20.932T - 1575.961$
	$A_5(T) = -14.338T - 8078.906$	$A_6(T) = -70.776T + 8898.941$

Parameter	Simulation value	Physical value	Parameter	Simulation value	Pshysical value
dt	0.2	$1.2 \cdot 10^{-5}$ s	T_m	0.99937	331.79 K
D_L	0.62	$10^{-9}\,\mathrm{m^2 s^{-1}}$	$\zeta_{\alpha\beta}$	in range of	-
$D_\alpha, D_\beta, D_\delta$	0	0		0.025 - 0.045	
ω	$3.24 \cdot 10^{-7}$	$0.309°s^{-1}$	$\tau_{\alpha\beta}$	13.62	calculated
$\gamma_{0\alpha\beta}, \gamma_{0\beta\delta}, \gamma_{\beta L}$	$9.26 \cdot 10^{-4}$	$0.2888\,\mathrm{Jm^{-2}}$	$\tau_{\alpha\delta}$	21.68	from
$\gamma_{0\alpha\delta}, \gamma_{\alpha L}$	$2.78 \cdot 10^{-4}$	$0.0866\,\mathrm{Jm^{-2}}$	$\tau_{\alpha L}$	1.45	[32]
$\gamma_{\delta L}$	$4.63 \cdot 10^{-4}$	$0.1444\,\mathrm{Jm^{-2}}$ [58]	$\tau_{\beta L}$	2.73	
$\gamma_{\alpha\beta\delta}$	$15 \cdot \gamma_{\alpha\beta}$	–	$\tau_{\delta L}$	1.31	
dx	1	0.312 μm	A_0	0.001374	0.456 K
G^{DS}	$7.52 \cdot 10^{-6}$	8 $\mathrm{Kmm^{-1}}$ [7]	A	5.0	–
G^{RDS}	$7.4 \cdot 10^{-6}-$	$0.786-$	i	400	–
	$2.255 \cdot 10^{-4}$	240 $\mathrm{Kmm^{-1}}$	c_{limit}	5%	–
$T_{eut.}$	1	332 K [26]			

Phase name	Eutectic composition		
	c_{Bi} in mol-%	c_{In} in mol-%	c_{Sn} in mol-%
α	32.01	66.67	1.32
β	8.02	66.96	25.02
δ	14.84	39.21	45.95
Liquid	20.37	60.36	19.27

In this section, an extensive study on system behavior in various arrangements and configurations is presented, considering the case $\zeta > \zeta_{cr}$. As a starting point, a classical setup is revisited: the growth of a single solid grain within a liquid phase. The effect of anisotropy at the solid–liquid interface is investigated[1] based on the obtained results. In Fig. 10, the evolution of a single circular δ grain in the liquid for different ζ values is illustrated.

---

[1] The main focus of this article is on solid-solid inter faces. This is the only case where anisotropy in the solid–liquid interface is active, serving as a general stability-check case study. This configuration is considered because anisotropy directly governs observable growth patterns at the solid–liquid interface, more significantly than at solid-solid interfaces.
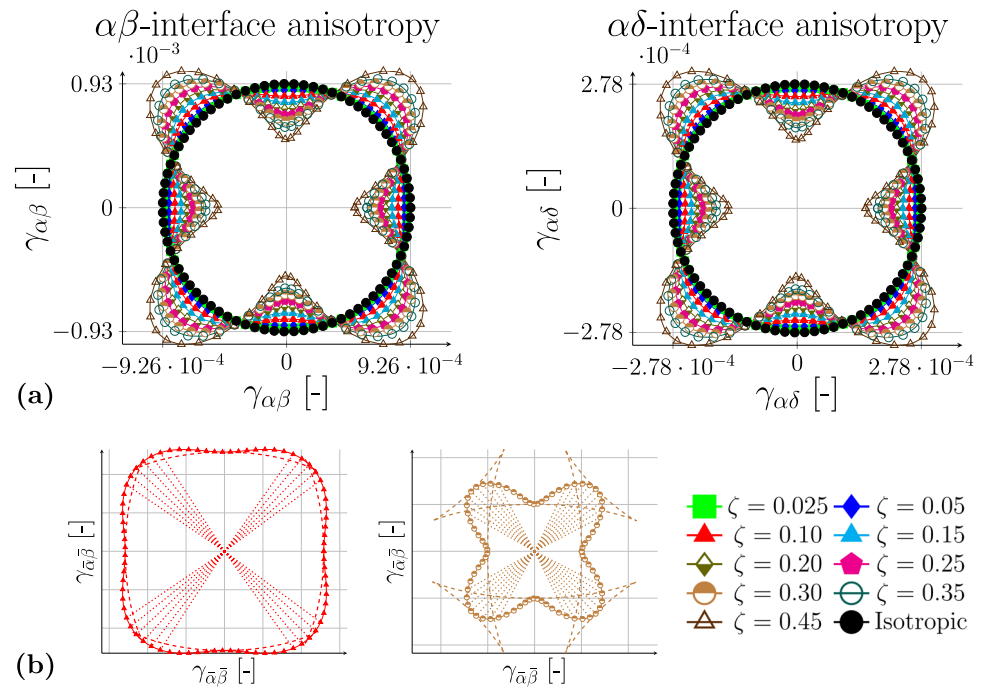
The study begins with the isotropic case and continues with anisotropic configurations, with $\zeta_{\delta L}$ ranging from the critical value 0.06 to the extreme value $\zeta = 0.35$. The temperature is maintained isothermally throughout the simulation domain, which contains a fixed solid circular grain embedded in the surrounding liquid. Micrographs are taken after a total of 1.25×10^6 time steps, ensuring consistent equilibrium states. The conserved composition dynamics alongside non-conserved phase-field dynamics are secured in the employed phase-field model described in section 2. The transformation of circular grains into square shapes is observed under different anisotropy conditions. To investigate interface properties, interface profiles at various angles are plotted. It is important to note that, unlike in RDS simulations, no field rotation exists in this case. The angles are defined using different Δx and Δy values, representing grid cell variation steps in the simulation. These measurements are taken from the point O, indicating the center of the simulation domain. The selected Δx and Δy values correspond to directions with at least three grid cells within the interface, ensuring meaningful profile analysis. For example, $\Delta x = 1, \Delta y = 0$ refers to the horizontal (x-axis) direction, and $\Delta x = 1, \Delta y = 1$ refers to 45°.

As shown in Fig. 10, the interface profiles in the isotropic simulation coincide in all directions, as expected. As $\zeta_{\delta L}$ increases, edge formation is observed at the four corners corresponding to minimum energy orientations, and these edges become sharper, causing directional variation in interface profiles. This variation becomes more pronounced with increasing anisotropy strength, although the smooth transition from 1 (δ bulk) to 0 (liquid) remains undistorted. At $\zeta_{\delta L} = 0.13$, nearly twice the reported ζ_{cr} in [51], simulation stability remains unaffected. At the extreme value $\zeta_{\delta L} = 0.35$, where facets appear in the Wulff plot and sharp corners indicate a loss of stability, the interface profiles across different angles remain consistent. The same solid–liquid modeling procedure is repeated for the β phase, and similar results are observed with the activation of $\zeta_{\beta L}$. Since the evolved microstructures are visually similar to those of δ grain growth, additional micrographs are not shown.

Next, a regular four-phase lamella initially filled with solid phases in the $\alpha\beta\alpha\delta$ arrangement is studied. The investigation begins with the DS setup, which represents the basic eutectic solidification simulation in the Bi-In-Sn system. In the isotropic simulation shown in Fig. 4 of [21], anisotropy is applied to the $\alpha\beta$ and $\alpha\delta$ interfaces with a strength of 0.45. The interface profiles are shown in Fig. 11 at growth distances of 40 μm ($\simeq 1.7 \cdot \lambda_{JH}$), 80 μm ($\simeq 3.5 \cdot \lambda_{JH}$), and 180 μm ($\simeq 7.5 \cdot \lambda_{JH}$). Sub-figure (a) corresponds

Figure 10 The evolution of the δ solid phase in the liquid at different anisotropy strengths. The interface width in different directions is plotted for each case..
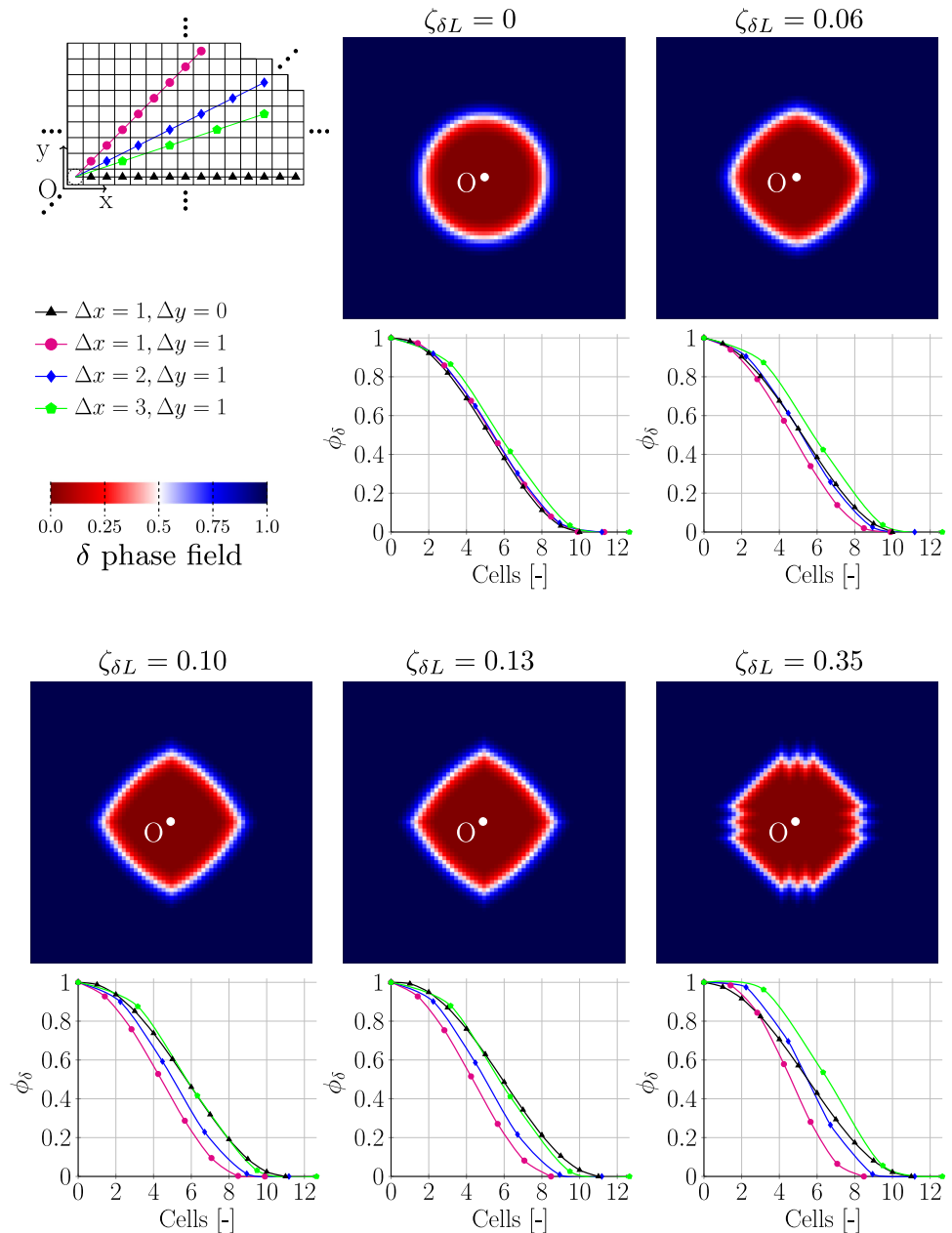
to $\alpha\beta$ anisotropy and sub-figure (b) to $\alpha\delta$ anisotropy. In both cases, interface stability is observed, indicating that the simulations remain stable over the studied growth distances.

In Fig. 12, an RDS simulation is presented where $\alpha\beta$ anisotropy with strength 0.45 is active. Measurements are performed after a $\pi/2$ radian rotation. The top and bottom plots show the Bi concentration and β phase-field, respectively. In the concentration plot, values of 8.02 mol%, 14.83 mol%, and 32 mol% correspond to the β, δ, and α phases, respectively.

Stable solid-solid interfaces are observed across different measured directions.

Figure 13 shows another RDS study where $\alpha\delta$ anisotropy with $\zeta_{\alpha\delta} = 0.25$ is activated. Similar stability is observed in this configuration as well.

A.1 Discussion

The simulations of the Bi-In-Sn system demonstrate stable growth for values of $\zeta > \zeta_{cr}$. The following factors contribute to this stability:

Figure 11 Interface profiles in concentration and phase fields: **a** $\alpha\beta$ anisotropy with $\zeta_{\alpha\beta} = 0.45$ and **b** $\alpha\delta$ anisotropy with $\zeta_{\alpha\delta} = 0.45$..
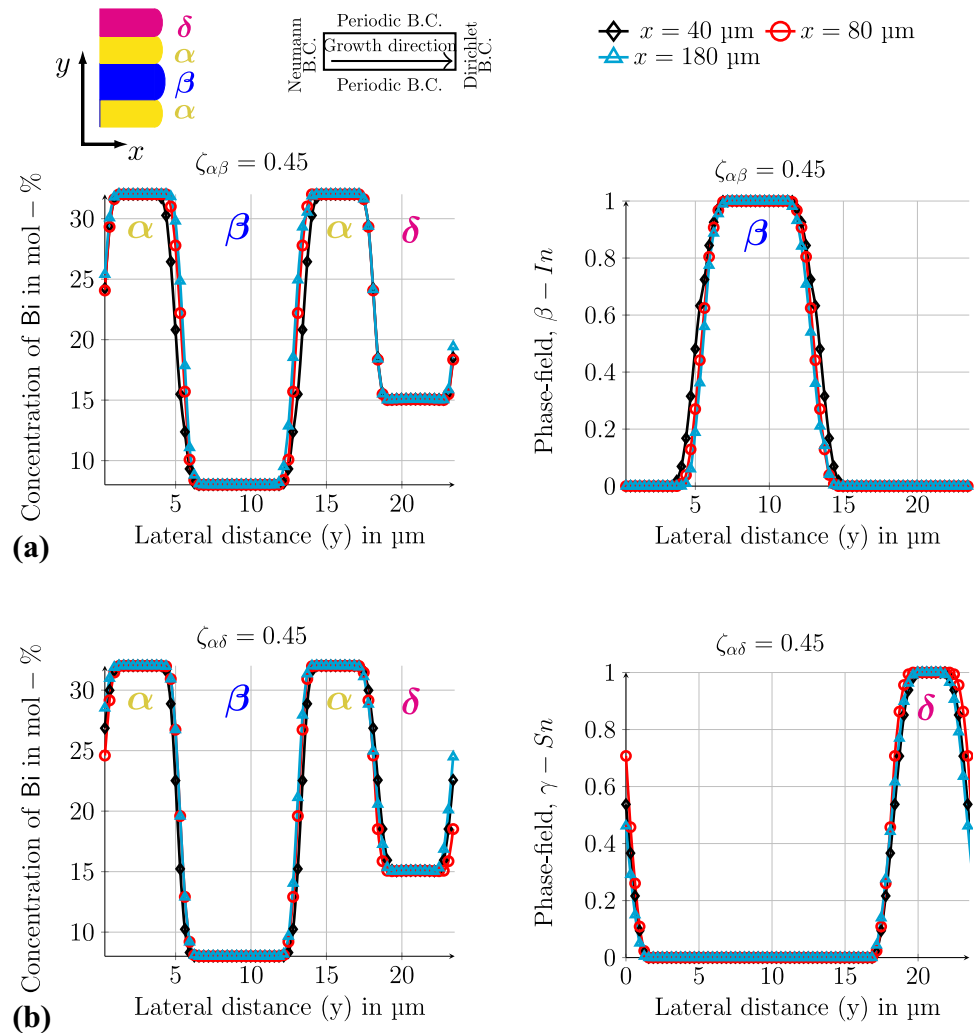
(i)   In the DS setup shown in Fig. 11, assuming the $+x$ axis as the growth direction (left to right), the solid-solid interfaces align along the x axis. The interface normals thus point in the $\pm y$ directions within the solidified phases. This alignment ensures that the system grows along energetically favorable directions (e.g., $\theta = 0$ in Fig. 9(a)), corresponding to regions of positive interface stiffness. As a result, the solidification front can remain smooth, stable, and regular, even for large ζ values, maintaining lamellar alignment.

(ii) In RDS simulations, the thermal gradient G^{RDS} rotates about the disk center (see Fig. 5 in [21]). Consequently, the crystallographic orientation (and hence $\gamma(\theta)$) rotates relative to the growth direction, creating a misalignment between the growth direction and the Wulff-plot minimum. However, due to the low rotation speed (slow enough to ensure equilibrium), the interface can remain near low-energy orientations during each small time step, avoiding regions with $S(\theta) < 0$ and preserving stability.

(iii) The real material system used in this study is modeled with precise parameters, including thermodynamic data from the CALPHAD database (see Section 3.1 in [21]), interfacial energy values aligned with Jackson–Hunt predictions (see Section 3.4 in [21]), and realistic diffusion coefficients. These accurate inputs result in stable simulations that match experimental behavior, even if the

mathematical stiffness criteria is not strictly satisfied.

(iv) From a numerical standpoint, despite the high nominal values of ζ, the model may include formulations that suppress negative stiffness regions at interfaces. This is likely achieved by incorporating higher-order terms such as the anti-third-phase term ($\gamma_{\hat{\alpha}\hat{\beta}\hat{\delta}}$ in $w(\phi)$ of Eq. (1)) and the anti-trapping current (J_{at} in Eq. (2)) to regulate interface width. A fine mesh resolution is also used to ensure accurate spatial discretization.

It is worth noting that for directions with negative stiffness, various numerical techniques have been introduced in the literature, such as applying moderate anisotropy with controlled smoothing [54] and including higher-order terms in phase-field models (e.g., $\kappa(\nabla^2\phi)^2$ [55]). These methods help to stabilize interface evolution by smoothing sharp corners and limiting excessive curvature. Such modifications are necessary in studies that report instabilities for $\zeta > \zeta_{cr}$.
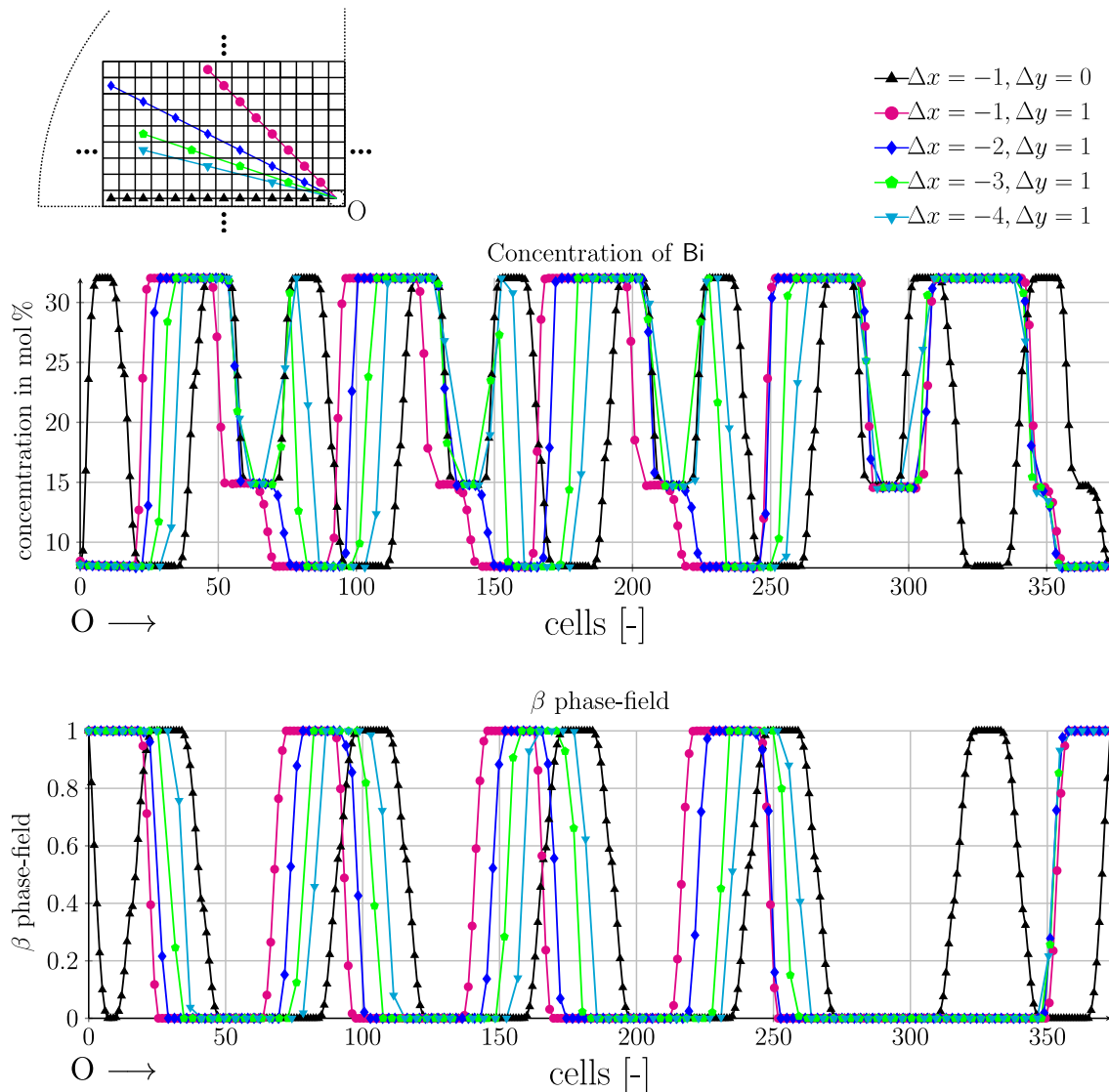
Appendix B Simulation parameters

Figure 12 Evolved interface profiles from an RDS simulation with $\zeta_{\alpha\beta} = 0.45$. Concentration (top) and β phase (bottom) fields are shown, illustrating interface behavior at various angles..
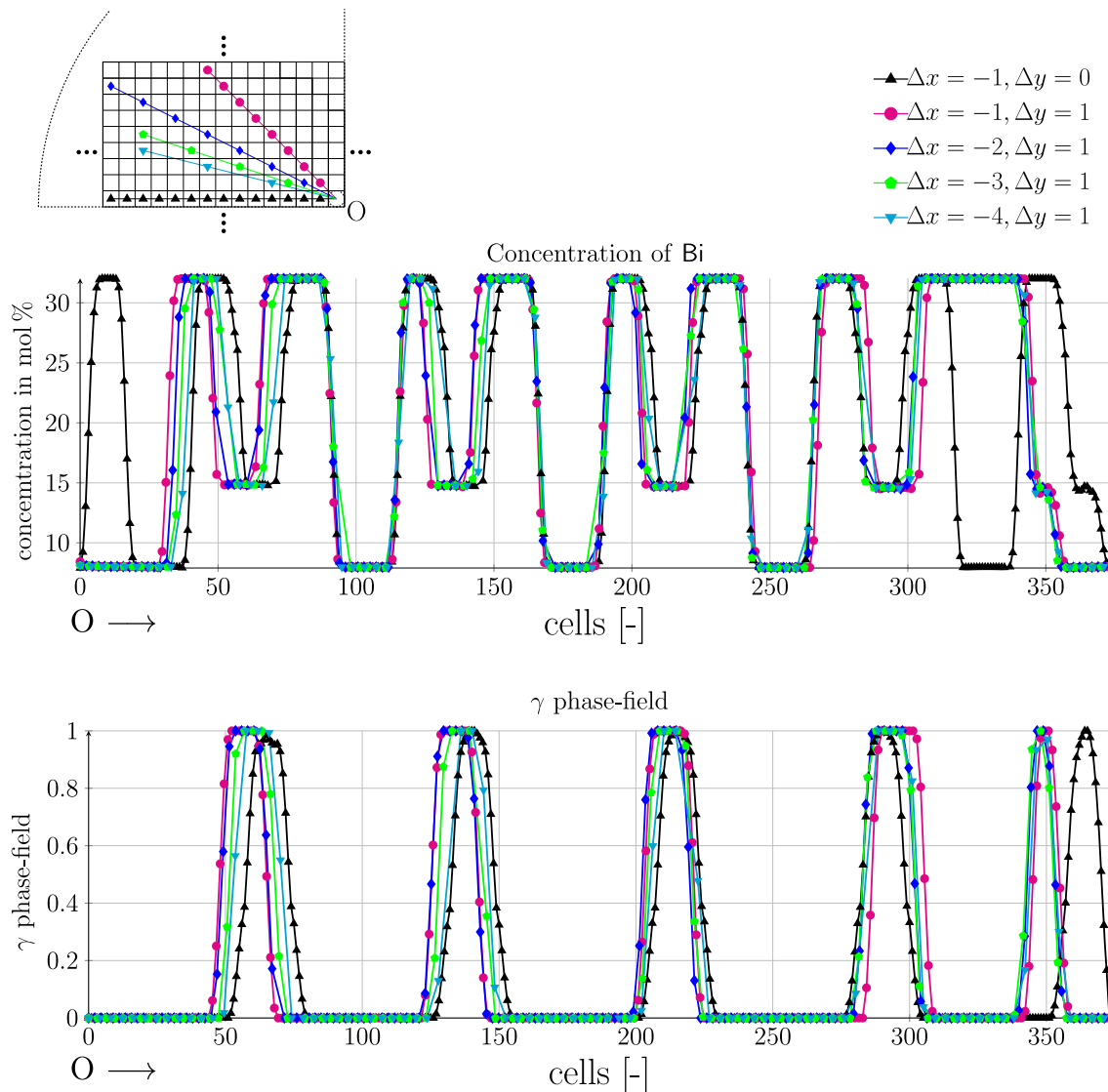
Figure 13 Evolved interface profiles from an RDS simulation with $\zeta_{\alpha\delta} = 0.25$. Concentration (top) and γ phase (bottom) fields are shown, demonstrating interface stability across different orientations..

References

[1] Hoyle R, McFadden G, Davis S (1996) Pattern selection with anisotropy during directional solidification. Philos Trans R Soc London Ser A Math Phys Eng Sci 354(1721):2915–2949

[2] Norris SA, Davis SH, Watson SJ, Voorhees PW (2008) Faceted interfaces in directional solidification. J Cryst Growth 310(2):414–427

[3] Ming-Wen C, Man L, Lin Y, Yu-Yan W, Zi-Dong W, Jian-Jun X (2009) The effect of anisotropic surface tension on the morphological stability of planar interface during directional solidification. Chin Phys B 18(4):1691

[4] Wang LL, Wang ZJ, Lin X, Wang M, Huang WD (2012) The effect of interfacial energy anisotropy on planar interface instability in a succinonitrile alloy under a small temperature gradient. Chin Phys B 21(6):066801

[5] Zhang J, Jun S, Shang Z, Lei W, Fu H (2013) Directional solidification and characterization of NiAl-9 Mo eutectic alloy. Trans Nonferrous Metals Soc China 23(12):3499–3507

[6] Ruggiero M, Rutter J (1997) Origin of microstructure in the 332 K eutectic of the Bi–In–Sn system. Mater Sci Technol 13(1):5–11

[7] Witusiewicz V, Hecht U, Rex S, Apel M (2005) In situ observation of microstructure evolution in low-melting Bi–

In–Sn alloys by light microscopy. Acta Mater 53(13):3663–3669

[8] Rex S, Böttger B, Witusiewicz V, Hecht U (2005) Transient eutectic solidification in In–Bi–Sn: two-dimensional experiments and numerical simulation. Mater Sci Eng, A 413:249–254

[9] Bottin-Rousseau S, Şerefoğlu M, Yücetürk S, Faivre G, Akamatsu S (2016) Stability of three-phase ternary-eutectic growth patterns in thin sample. Acta Mater 109:259–266

[10] Mohagheghi S, Şerefoğlu M (2017) Dynamics of spacing adjustment and recovery mechanisms of ABAC-type growth pattern in ternary eutectic systems. J Cryst Growth 470:66–74

[11] Woodruff DP, Ward I (1973) The Solid-liquid Interface. Cambridge University Press UK 1:77–100

[12] Karma A (1987) Beyond steady-state lamellar eutectic growth. Phys Rev Lett 59(1):71

[13] Kassner K, Valance A, Misbah C, Temkin D (1993) New broken-parity state and a transition to anomalous lamellae in eutectic growth. Phys Rev E 48(2):1091

[14] Karma A, Sarkissian A (1996) Morphological instabilities of lamellar eutectics. Metall Mater Trans A 27(3):635–656

[15] Mohagheghi S, Şerefoğlu M (2018) Quasi-isotropic and locked grain growth dynamics in a three-phase eutectic system. Acta Mater 151:432–442

[16] Oswald P, Moulin M, Metz P, Géminard J-C, Sotta P, Sallen L (1993) An improved directional growth apparatus for liquid crystals: applications to thermotropic and lyotropic systems. J Phys III 3(9):1891–1907

[17] Akamatsu S, Bottin-Rousseau S, Şerefoğlu M, Faivre G (2012) Lamellar eutectic growth with anisotropic interphase boundaries: experimental study using the rotating directional solidification method. Acta Mater 60(6–7):3206–3214

[18] Zhao Y (2023) Understanding and design of metallic alloys guided by phase-field simulations. NPJ Comput Mater 9(1):94

[19] Zhao Y, Xin T, Tang S, Wang H, Fang X, Hou H (2024) Applications of unified phase-field methods to designing microstructures and mechanical properties of alloys. MRS Bull 49(6):613–625

[20] Noubary KD, Kellner M, Hötzer J, Seiz M, Seifert HJ, Nestler B (2021) Data workflow to incorporate thermodynamic energies from Calphad databases into grand-potential-based phase-field models. J Mater Sci 56(20):11932–11952. https://doi.org/10.1007/s10853-021-06033-7

[21] Dargahi Noubary K, Kellner M, Nestler B (2022) Rotating directional solidification of ternary eutectic microstructures in Bi–In–Sn: a phase-field study. Materials 15(3):1160. https://doi.org/10.3390/ma15031160

[22] Hötzer J, Reiter A, Hierl H, Steinmetz P, Selzer M, Nestler B (2018) The parallel multi-physics phase-field framework Pace3D. J Comput Sci 26:1–12

[23] Software Package Parallel Algorithms for Crystal Evolution in 3 D—Pace3D. [Accessed: August 2025]. https://www.h-ka.de/en/idm/profile/pace3d-software

[24] Andersson JO, Helander T, Höglund L, Shi P, Sundman B (2002) Thermo—Calc & DICTRA, computational tools for materials science. Calphad 26(2):273–312

[25] Peng J, Franke P, Seifert HJ (2016) Experimental investigation and Calphad assessment of the eutectic trough in the system NiAl–Cr–Mo. Phase Equilibria Diff 37(5):592–600

[26] Witusiewicz VT, Hecht U, Böttger B, Rex S (2007) Thermodynamic re-optimisation of the Bi–In–Sn system based on new experimental data. J Alloy Compd 428(1–2):115–124

[27] Dejmek M, Folch R, Parisi A, Plapp M (2004) Three-dimensional phase-field simulations of directional solidification. arXiv preprint arXiv: cond-mat/0401250

[28] Ma W, Li R, Chen H (2020) Three-dimensional ca-lbm model of silicon facet formation during directional solidification. Curr Comput-Aided Drug Des 10(8):669

[29] Gurevich S, Karma A, Plapp M, Trivedi R (2010) Phase-field study of three-dimensional steady-state growth shapes in directional solidification. Phys Rev E-Stat Nonlinear Soft Matter Phys 81(1):011603

[30] Hunt J, Jackson K (1966) Lamellar and rod eutectic growth. Trans Metall Soc AIME 236:1129–1142

[31] Plapp M (2011) Unified derivation of phase-field models for alloy solidification from a grand-potential functional. Phys Rev E 84(3):031601

[32] Choudhury A, Nestler B (2012) Grand-potential formulation for multicomponent phase transformations combined with thin-interface asymptotics of the double-obstacle potential. Phys Rev E 85(2):021602

[33] Bauer M, Hötzer J, Jainta M, Steinmetz P, Berghoff M, Schornbaum F, Godenschwager C, Köstler H, Nestler B, Rüde U (2015) Massively parallel phase-field simulations for ternary eutectic directional solidification. In: Proceedings of the International Conference for High Performance Computing, Networking, Storage and Analysis, pp. 1– 12

[34] Hötzer J, Tschukin O, Said MB, Berghoff M, Jainta M, Barthelemy G, Smorchkov N, Schneider D, Selzer M, Nestler B (2016) Calibration of a multi-phase field model with quantitative angle measurement. J Mater Sci 51(4):1788–1797

[35] Hötzer J, Jainta M, Steinmetz P, Nestler B, Dennstedt A, Genau A, Bauer M, Köstler H, Rüde U (2015) Large scale phase-field simulations of directional ternary eutectic solidification. Acta Mater 93:194–204

[36] Steinmetz P, Yabansu YC, Hötzer J, Jainta M, Nestler B, Kalidindi SR (2016) Analytics for microstructure datasets produced by phase-field simulations. Acta Mater 103:192–203

[37] Noubary KD, Kellner M, Steinmetz P, Hötzer J, Nestler B (2017) Phase-field study on the effects of process and material parameters on the tilt angle during directional solidification of ternary eutectics. Comput Mater Sci 138:403–411. https://doi.org/10.1016/j.commatsci.2017.07.006

[38] Dargahi Noubary K, Schäfer C, Pauly C, Kellner M, Ott V, Stüber M, Mücklich F, Nestler B (2023) Microstructure evolution in the self-propagating reaction in al/ru bilayers by phase-field simulations and experiments. J Vacuum Sci Technol A. https://doi.org/10.1116/6.0002587

[39] Moelans N (2011) A quantitative and thermodynamically consistent phase-field interpolation function for multi-phase systems. Acta Mater 59(3):1077–1086. https://doi.org/10.1016/j.actamat.2010.10.038

[40] Schoof E, Schneider D, Streichhan N, Mittnacht T, Selzer M, Nestler B (2018) Multiphase-field modeling of martensitic phase transformation in a dual-phase microstructure. Int J Solids Struct 134:181–194

[41] Kellner M, Hötzer J, Schoof E, Nestler B (2020) Phase-field study of eutectic colony formation in Ni Al-34 Cr. Acta Mater 182:267–277

[42] Hinrichs F, Kellner M, Hötzer J, Nestler B (2020) Calibration of a concentration-driven nucleation mechanism for phase-field simulations of eutectic and off-eutectic compositions in AlCu-5 Ag. Scripta Mater 186:89–94

[43] Kellner M, Hierl H, Nestler B(2024) Influence of the phase fractions on the formation of eutectic colonies: a large-scale phase-field study. Adv Eng Mater, 2301766

[44] Kellner M, Sprenger I, Steinmetz P, Hötzer J, Nestler B, Heilmaier M (2017) Phase-field simulation of the microstructure evolution in the eutectic NiAl-34 Cr system. Comput Mater Sci 128:379–387

[45] Kellner M, Kunz W, Steinmetz P, Hötzer J, Nestler B (2018) Phase-field study of dynamic velocity variations during directional solidification of eutectic NiAl-34 Cr. Comput Mater Sci 145:291–305

[46] Mohagheghi S, Şerefoğlu M (2019) On the growth dynamics of nearly-locked grain in the three-phase in–bi–sn eutectic system. Metall Mater Trans A 50:5221–5233

[47] Garcke H, Stoth B, Nestler B (1999) Anisotropy in multi-phase systems: a phase field approach. Interfaces Free Bound 1(2):175–198

[48] Mohagheghi S, Şerefoğlu M (2024) On the effect of inter-phase boundary energy anisotropy on morphologies: A new type of eutectic grain observed in a three-phase eutectic system. Metall Mater Trans A, 1–14

[49] Nestler B, Garcke H, Stinner B (2005) Multicomponent alloy solidification: phase-field modeling and simulations. Phys Rev E 71(4):041609

[50] Tschukin O, Silberzahn A, Selzer M, Amos PG, Schneider D, Nestler B (2017) Concepts of modeling surface energy anisotropy in phase-field approaches. Geothermal energy 5:1–21

[51] Kobayashi R (1993) Modeling and numerical simulations of dendritic crystal growth. Phys D 63(3):410–423

[52] Karma A, Rappel W-J (1996) Phase-field method for computationally efficient modeling of solidification with arbitrary interface kinetics. Phys Rev E 53(4):3017

[53] Taylor JE, Cahn JW, Handwerker CA (1992) Overview no. 98 i-geometric models of crystal growth. Acta Metall Mater 40(7):1443–1474

[54] Eggleston JJ, McFadden GB, Voorhees PW (2001) A phase-field model for highly anisotropic interfacial energy. Phys D 150(1–2):91–103

[55] Wise S, Kim J, Lowengrub J (2007) Solving the regularized, strongly anisotropic cahn-hilliard equation by an adaptive nonlinear multigrid method. J Comput Phys 226(1):414–446

[56] Noubary MSKD (2022) Effects of anisotropy of the interfacial energies on pattern formation within solidification of ternary eutectics: A phase-field study. PhD thesis, Karlsruhe Institute of Technology

[57] Hu L, Hu W, Gottstein G, Bogner S, Hollad S, Bührig-Polaczek A (2012) Investigation into microstructure and mechanical properties of NiAl–Mo composites produced by directional solidification. Mater Sci Eng, A 539:211–222

[58] Akbulut S, Ocak Y, Maraşlı N, Keşlioğlu K, Kaya H, Çadırlı E (2009) Determination of interfacial energies of solid Sn solution in the In–Bi–Sn ternary alloy. Mater Charact 60(3):183–192